Int. J. Multiphase Flow Vol. 19, No. 6, pp. 1093–1127, 1993
Printed in Great Britain.

0301-9322/93 $6.00 + 0.00

CHARACTERIZATION OF PARTICLE-LADEN, CONFINED SWIRLING FLOWS BY PHASE-DOPPLER ANEMOMETRY AND NUMERICAL CALCULATION

M. SOMMERFELD and H.-H. QIU
Lehrstuhl für Strömungsmechanik, Universität Erlangen/Nürnberg, Cauerstr. 4, 91058 Erlangen, Germany

(Received 14 December 1992; in revised form 8 August 1993)

Abstract—The particle dispersion characteristics in a confined swirling flow with a swirl number of approx. 0.5 were studied in detail by performing measurements using phase-Doppler anemometry (PDA) and numerical predictions. A mixture of gas and particles was injected without swirl into the test section, while the swirling airstream was provided through a co-flowing annular inlet. Two cases with different primary jet exit velocities were considered. For these flow conditions, a closed central recirculation bubble was established just downstream of the inlet.

The PDA measurements allowed the correlation between particle size and velocity to be obtained and also the spatial change in the particle size distribution throughout the flow field. For these results, the behaviour of different size classes in the entire particle size spectrum, ranging from about 15 to 80 μm, could be studied, and the response of the particles to the mean flow and the gas turbulence could be characterized. Due to the response characteristics of particles with different diameters to the mean flow and the flow turbulence, a considerable separation of the particles was observed which resulted in a streamwise increase in the particle mean number diameter in the core region of the central recirculation bubble. For the lower particle inlet velocity (i.e. low primary jet exit velocity), this effect is more pronounced, since here the particles have more time to respond to the flow reversal and the swirl velocity component. This also gave a higher mass of recirculating particle material.

The numerical predictions of the gas flow were performed by solving the time-averaged Navier–Stokes equations in connection with the well known k–ϵ turbulence model. Although this turbulence model is based on the assumption of isotropic turbulence, the agreement of the calculated mean velocity profiles compared to the measured gas velocities is very good. The gas-phase turbulent kinetic energy, however, is considerably underpredicted in the initial mixing region. The particle dispersion characteristics were calculated by using the Lagrangian approach, where the influence of the particulate phase on the gas flow could be neglected, since only very low mass loadings were considered. The calculated results for the particle mean velocity and the mass flux are also in good agreement with the experiments. Furthermore, the change in the particle mean diameter throughout the flow field was predicted approximately, which shows that the applied simple stochastic dispersion model also gives good results for such very complex flows. The variation of the gas and particle velocity in the primary inlet had a considerable impact on the particle dispersion behaviour in the swirling flow and the particle residence time in the central recirculation bubble, which could be determined from the numerical calculations. For the lower particle inlet velocity, the maximum particle size-dependence residence time within the recirculation region was considerably shifted towards larger particles.

Key Words: swirling flow, particle dispersion, phase-Doppler anemometry, numerical calculations, Euleridu Lagrangian approach

INTRODUCTION

Swirling two-phase flows are encountered in a variety of forms in many engineering applications. In industrial processing plants, for example, cyclone separators are used to clean a fluid stream from solid particles. Here, the mechanism for the separation of the particles is the centrifugal force exerted on the particle in the swirling flow of the cyclone.

In combustion systems, the special features of swirling flows are used to establish high mixing rates between the fuel (natural gas, liquid fuel or pulverized coal) and the swirling air stream, and to enhance the flame stability. Flame stabilization is obtained by a central recirculation zone, the resulting upstream convection of hot reaction products and the resulting mixing with the incoming fuel and air stream. The occurrence of a central recirculation zone observed above a certain critical swirl intensity is usually referred to as vortex breakdown (Escudier & Keller 1985).

To improve the understanding of the aerodynamics of isothermal swirling flows, a number of detailed studies have been carried out in the past (Lilley 1977; Altgeld *et al.* 1983; Rhode *et al.* 1983; Hallett & Toews 1987; Dellenback *et al.* 1988). The main objective of these studies was to characterize this complex flow and to reveal the influence of the burner geometry and fluid dynamic boundary conditions on the development of the central reverse flow region. Furthermore, numerous studies have been conducted on the aerodynamics of combusting swirling flows (e.g. Lilley 1977; Syred & Beer 1974; Brum & Samuelsen 1987) in order to reveal the influence of combustion on the flow structure. All of these studies showed that the flow structure under combusting conditions deviates considerably from that of isothermal swirling flows, and that the latter are only useful for designing swirl burners in the first approach. The effect of the established flame type on the resulting NO_x emission has been discussed recently by Thielen (1988). In addition, some experiments have been performed in pulverized-coal-fuelled burners and boilers (e.g. Pröbstle & Wenz 1988).

Compared to the large body of publications with reacting and non-reacting swirling flows, only a few publications deal with particle or droplet motion and dispersion in swirling flows (Blümcke *et al.* 1988; Bulzan *et al.* 1988; Hardalupas *et al.* 1990; Sommerfeld & Krebs 1990; Sommerfeld & Qiu 1991). Recently, measuring techniques like laser- or phase-Doppler anenometry (LDA or PDA) allow for much more detailed information on the particle behaviour in such complex flows.

In recent publications by Blümcke *et al.* (1988), the understanding of droplet dispersion in a turbulent, confined swirling flow has been improved by both experimental and numerical studies. The dispersion of a droplet chain produced by a vibrating orifice was recorded by in-line holography and the velocity characteristics were determined by LDA. The numerical calculations of the particle dispersion by Blümcke *et al.* (1988) were performed by a newly developed spectral dispersion model for the droplets based on the measured gas flow field. The agreement between the measured and calculated dispersion characteristics was found to be reasonably good.

In the work of Bulzan *et al.* (1988), only weakly swirling free jets have been considered where no central recirculation was established. Their measurements were performed using both LDA and PDA.

The size–velocity correlation of droplets dispersing in a liquid-fuelled swirl burner was studied recently by Hardalupas *et al.* (1990) using PDA. Their results demonstrate the behaviour of different-sized droplets in a swirling free jet eminating from a quarrel-type burner nozzle under combusting and isothermal conditions. Measurements could, however, only be performed in the free jet downstream the quarrel. Since the kerosine droplets were directly injected into the swirling air stream inside the quarrel, the downstream-measured radial profiles of the droplet mean number diameter show a minimum in the jet core of the non-reacting flow. The larger droplets, which already show higher radial velocities just downstream of the quarrel, are centrifuged out of the core region. Under combustion conditions this effect is slightly modified owing to droplet evaporation. The distribution of the particle mass flux showed maximum values near the edge of the spray for both conditions. Consideration of the droplet velocity charcteristics shows that the velocity fluctuations of the smaller droplets are always higher than those of the larger droplets, since they are able to respond more easily to the gas turbulence. The gas velocity, however, was not measured in the study of Hardalupas *et al.* (1990).

In a very recent study by Brena de la Rosa *et al.* (1992), the influence of swirl intensity on the dispersion of a liquid spray in a confined swirling flow was examined using PDA. This measuring technique allowed the determination of the velocity characteristics of different-sized droplets and the evolution of the droplet mean diameter and the volume flux throughout the flow field. The turbulence characteristics of the air flow were measured by seeding the flow additionally with micron-sized liquid droplets.

In a preliminary study by Sommerfeld & Krebs (1990), the effect of swirl on the dispersion of solid particles in a confined swirling flow was studied in comparison to the non-swirling case. The measurements were performed by applying LDA. In these experiments, spherical glass beads with a mean number diameter of 108 μm and a narrow size distribution were used. This implies that all the particles behave in the same way, namely, that of a monodisperse phase. Due to the rather large particle diameter, however, the particle behaviour in the swirling flow was mainly governed by inertial effects, and it was found that the particles completely traverse the central recirculation bubble without a considerable spreading of the particle jet. The central recirculation region showed an annular shape, which was the result of the area contraction mounted at the end of the test section.

In continuation of this study (Sommerfeld & Qiu 1991; Sommerfeld *et al.* 1991), the area contraction was removed and a settling chamber was placed at the end of the test section. This, finally, gave a closed central recirculation bubble. Furthermore, smaller particles with a mean number diameter of 45 μm and a size spectrum between 15–80 μm were used in these experiments in order to obtain a better response of the particles to the fluid flow and simulate a more realistic situation, e.g. as found in pulverized coal burners. Gas and particle velocity characteristics were measured by employing PDA, which, additionally, allows the measurement of the particle size–velocity correlation. This measuring technique enables studies of the behaviour of different particle size classes within the size spectrum of the particle material used. Furthermore, the change in the particle size distribution throughout the flow field was studied, which indicated strong separation effects due to radial transport, turbulent diffusion and the action of centrifugal forces.

The numerical prediction of swirling flows is rather difficult due to the large velocity gradients in these flows, which result in a strong anisotropy of the turbulence. Therefore, higher-order turbulence models are preferable for predicting swirling flows. Recently, a number of studies have been performed where Reynold-stress turbulence models have been applied to the simulation of swirling free jets (Fu *et al.* 1988) and confined swirling flows (Hogg & Leschziner 1989; Weber *et al.* 1990). The comparison of these results with predictions based on the well-known k–ϵ turbulence model showed that this simpler model is able to predict mean velocities reasonably well in some cases. The normal Reynolds stresses are, however, considerably overpredicted in these studies (Hogg & Leschziner 1989; Weber *et al.* 1990) which is, of course, related to the assumption of isotropic turbulence associated with the k–ϵ turbulence model. A numerical study performed by Durst & Wennerberg (1991) revealed the limitations in predicting swirling flows via the k–ϵ turbulence model.

TEST FACILITY

For the detailed study of particle-laden, swirling two-phase flows, a vertical test section with a downward flow was chosen (figure 1). To allow good optical access, a simple pipe expansion was selected as the test section. Such a configuration has the advantage that the inlet conditions can be measured easily, which is important for performing numerical calculations. The complete test rig consists of two flow circuits [figure 1 (**5, 6**)] for the primary and secondary annular flows, respectively. A blower (**1**) with a variable flow rate supplies these two pipe systems via a T-junction and a throttle valve (**2**) is used to adjust the flow rate at the primary inlet. The mass flow rates through the primary and annular inlets were obtained from two orifice flow meters (**3**). The secondary flow circuit is split into four smaller pipes which are connected radially to the swirl generator. The upper part of the swirl generator is constructed as a settling chamber, and the air passes over a number of screens and then moves radially inward across the radial swirl vanes. The swirl intensity of the annular flow may be adjusted continuously by turning the swirl vanes in the radial swirl generator (**8**). The primary flow circuit is connected to a pipe passing straight through the center of the swirl generator. The dust particles are injected into the primary flow above the swirl generator by a particle feeder (**4**) with a variable-speed motor. Above the particle feeder, a reservoir (**7**) for the dust particles is installed.

The inlet configuration and the dimensions of the test section are also shown in figure 1. The test section consists of a 1.5 m long Plexiglas tube with an inner diameter of 194 mm. The end of the test section is connected to a stagnation chamber (**11**) because previous measurements (Sommerfeld & Krebs 1990) showed that an area contraction at the end of the test section has a signficant influence on the flow structure in the test section. As a result, an annular type of central recirculation bubble was established during these measurements. This is caused by the subcritical nature of isothermal swirling flows, where a contraction at the outlet may result in inertial waves propagating upstream, against the flow, and may considerably influence the flow structure (Escudier & Keller 1985).

The stagnation chamber is connected to a cyclone separator (**13**) and an additional paper filter to separate both the large and seeding particles, which are used as tracers for measuring the gas velocity. These tracer particles are injected into both pipe systems before the swirl generator. To

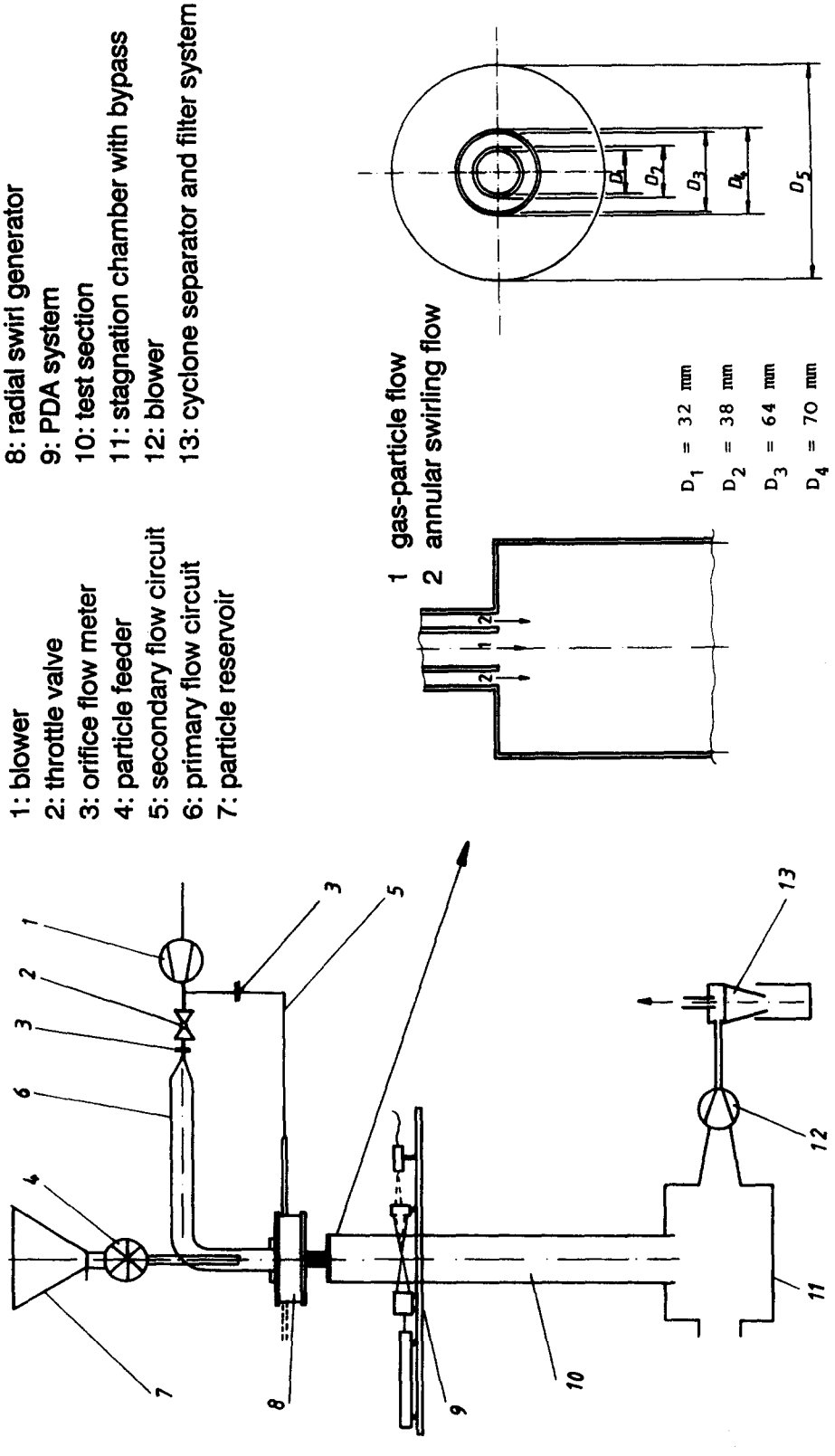

Figure 1. Test facility and dimensions of the test section (length: 1.5 m).

guarantee that the flow rate in the test section is independent of the pressure loss in the filter system, which may vary during the measurements, an additional blower (**12**) is used in connection with a bypass valve at the stagnation chamber (**11**).

Particle size and velocity measurements were performed at several cross-sections in the test section, including the inlet using a one-component PDA. In order to allow measurements of the three velocity components (axial velocity u, radial velocity v, and tangential velocity w), the PDA system was mounted on a stepper-motor-controlled three-dimensional traversing system (figure 1). To avoid strong laser-beam deflections and a realignment of the receiving optics for every measuring point, the Plexiglas test section has several slits which are covered from the inside by 100 μm thick glass plates. This results in negligible beam distortion, especially when the radial and axial velocities are measured, where the receiving optics have to be mounted in such a way that the optical axis of the receiving optics is oblique to the walls of the test section. For each velocity component, different test sections with different slit locations were used, which allowed the appropriate installation of the PDA receiving optics and the measurement of particle size–velocity correlation for each velocity component.

MEASURING TECHNIQUE

The PDA used for the present experiments is shown in figure 2, together with the data-processing equipment. The transmitting optics is a conventional system with two bragg cells, and a front lens with a 485 mm focal length was used. The relative shift frequency between the two beams was fixed at 2 MHz, which allows measurement of negative velocities up to 20 m/s. The PDA receiving optics were mounted at 30° off-axis from the forward scattering direction. This position was selected in order to have high scattering intensities for the seeding particles with reasonable signal-to-noise ratios (SNRs). For the measurement of the axial velocity and the radial and tangential velocities, the receiving optics were at different positions.

The collimating lens of the receiving optics module (focal length 310 mm) produces a parallel beam of scattered light which is partially blocked by two rectangular slits with a separation of 40 mm, allowing for an integration along the scattered fringe pattern and therefore diminishing diffraction effects in this near-forward scattering direction. Behind the mask with the rectangular slits a lens was located, which focuses the scattered light onto a pinhole. The light rays are made parallel by an achromatic lens with a focal length of 80 mm. A beam spacer is used to separate

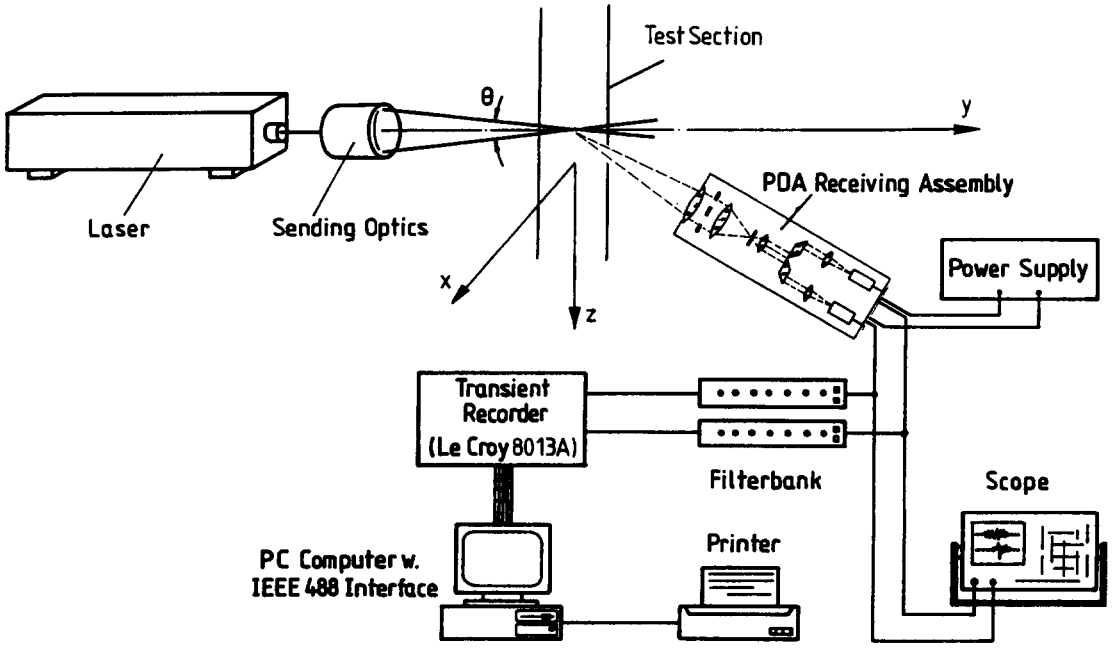

Figure 2. Optical system of the PDA and data acquisition system.

Table 1. Parameters of the PDA optical system

Transmitting optics	
Wavelength of the laser	632.8 nm
Diameter of the laser beam ($D_{e^{-2}}$)	1.0 mm
Focal length of the front lens	485 mm
Beam separation	30 mm
Diameter of the measuring volume	391 μm
Length of the measuring volume	12.6 mm
Fringe spacing	10.24 μm
Fringe number	38
Shift frequency	2 MHz
Conversion factor	10.24 m/s/MHz
Receiving optics	
Off-axis angle	30 deg
Focal length of the collimating lens	310 mm
Dimensions of the rectangular apertures	60 × 20 mm
Detector separation	40 mm
Focal length of the imaging lens	160 mm
Diameter of the pinhole	200 μm
Length of the measuring volume imaged onto the photodiodes	775 μm
Phase conversion factor	−2.93 deg/μm

the scattered light from the two rectangular apertures, which is then focused onto two avalanche-photodiodes in the receiving optics module. All dimensions and characteristics of the optical system are summarized in table 1. With this optical configuration of the PDA system, the size of glass beads up to 123.8 μm could be measured.

The signals from the two avalanche-photodiodes are band-pass filtered and stored in a 200 MHz, two-channel transient recorder (type: Le Croy 8013 A). The transient recorder is operated in a sequential mode, where the total memory of 32 kbyte for each channel was divided into 400 segments by an external trigger unit. After storage of the 400 burst pairs, the data are transferred to a PC (type: Compaq 386/25) by an IEEE-488 interface card. While the data are processed in the PC, the transient recorder is armed again and the next 400 burst pairs are acquired and stored in the transient recorder. Using the procedure described above, it was possible to achieve effective data rates of about 50 Hz for digitizing, acquisition and subsequent processing. The maximum data rate for signal storage in the transient recorder is about 50 kHz.

The software data processing for estimating the signal frequency and the phase between the two signals is based on the cross-spectral density (CSD) function in connection with a fast-Fourier transform (FFT) (Domnick *et al.* 1988), which was recently modified to yield higher accuracy for the velocity estimation by using a "five-point" interpolation between the discrete frequency lines (Qiu *et al.* 1991). Especially in recirculating flows, accuracies of about 0.1 m/s are necessary to accurately resolve the spatial location of the recirculation regions. The FFT-length was set to 64 points with a sampling frequency of 12.5 MHz. This rather short FFT-length gave high processing speeds, and accuracies between 0.07 and 0.15 m/s could be achieved for the velocity estimation by using the five-point interpolation to the discrete frequency lines in the spectrum. The accuracy for size estimation using the five-point interpolation method was in the range 0.8–0.25 μm. These values cover the range of the SNRs measured for the seeding and dispersed-phase particles in the present situation. More details about the accuracy of the data processing, which strongly depends on the SNR, are given by Qiu *et al.* (1991).

In order to allow simultaneous measurements of gas and particle velocities, the flow was additionally seeded with small, spherical tracer particles (ballotini, type 7000). Since the size distribution of the particles ranges up to about 10 μm, a phase discrimination procedure was employed which insured that only tracer particles up to a maximum of 4 μm are sampled for determining the gas velocity. This procedure resulted in a mean diameter of about 1.5 μm for the validated signals from the tracer particles. A detailed description of the phase discrimination procedure was given previously by Sommerfeld & Qiu (1991) and Qiu *et al.* (1991).

The particle mass flux was measured separately with the single-detector receiving system. The receiving optics were positioned 90° off-axis from the forward scattering direction in order to obtain an exact demarcation of the measuring volume. At each measuring point, the number of particles

N traversing the control volume were counted within a certain time period Δt, and the particle velocity was measured simultaneously. For these measurements the transient recorder was also operated in the sequential mode, which ensured a real-time data acquisition, at least for the particle concentrations considered. During the storage of the 400 events, an internal clock was used to determine the effective measuring time. The total particle mass flux is then obtained with the cross-section of the control volume A_c, which was calculated from the optical configuration

$$f_p = \frac{N\bar{m}_p}{\Delta t A_c}, \qquad [1]$$

where N, Δt and $\bar{m}_p$ are the counted number of particles, the total measuring time and the mean particle mass, respectively. The mean particle mass at a certain measuring location was calculated from the volume mean particle diameter obtained from the PDA size measurements. Due to the uncertainties in the determination of the cross-section of the control volume, the measured mass flux was corrected using the global mass balance. The total measured particle mass flow rate was obtained by integrating the mass flux profile at the inlet. In comparison with the global mass flow rate obtained by weighting the particles collected during a certain time period in the cyclone separator, a correction factor was determined and applied to the mass flux measurements at all other cross-sections. The integration of the measured and corrected mass flux profiles revealed that the error in the particle mass flow rate was in the range $\pm 20\%$ for the various profiles. This rather large error was caused mainly by the poor resolution of the measurements in the near-wall region, where the integration area is the largest in the circular cross-section of the pipe. Furthermore, the particle mass flux was separated to give the positive and negative fluxes, which gives additional information about the mass and number of particles having negative velocities. For this separation, the particle volume mean diameter for particles with only positive and negative axial velocity was determined from the PDA measurements.

Measurements of the three velocity components were conducted at 8 cross-sections downstream of the inlet. At each measuring location, 2000 samples were taken to obtain the gas velocity and the associate r.m.s. values. In order to achieve reasonably accurate velocity statistics for the particle phase in the different size classes, 18,000 samples were acquired. The total measuring time for each location was between 15–30 min, which was strongly dependent on the local particle concentration. The maximum measurable particle size range between 0–123.8 μm was resolved by 40 classes, each 3.1 μm in width. Besides the information on the change in the particle size distribution throughout the flow field, the stored data of particle size and velocity could be reprocessed after the measurement in order to give the particle velocity in certain size classes.

FLOW CONDITIONS

In the present experiments, two flow conditions with different flow rates at the particle-laden primary inlet were considered. The resulting maximum gas velocities for the two cases were 12.5 and 7.4 m/s, respectively. The flow rate in the annular inlet was adjusted to give a maximum velocity of about 18 m/s. The maximum tangential velocity was, for both cases, about 13 m/s, which corresponds to a swirl vane angle of 30°.

The associated mass flow rates for the gas and the particles, the flow Reynolds number, the swirl number and other experimental conditions are listed in table 2. The mass flow rates of the primary and secondary annular jets were calculated from the pressure drops across the orifice flow meters. The flow Reynolds number was obtained with the total volume flow rate at the inlet and the outer diameter of the annulus ($D_3 = 64$ mm). The swirl number was calculated as the ratio of the axial flux of angular momentum to the axial flux of linear momentum, which were obtained by integration across both the primary and annular inlets. The following definition of the swirl number was used:

$$S = \frac{2\int_0^{D_3/2} \rho W U r^2 \, dr}{D_5 \int_0^{D_3/2} \rho U^2 r \, dr}, \qquad [2]$$

Table 2. Flow conditions and particle properties

	Case 1	Case 2
Air flow		
Mass flow rate of the primary jet (g/s)	9.9	6.0
Mass flow rate of the secondary jet (g/s)	38.3	44.6
Inlet Reynolds number (with $D_3 = 64$ mm)	52400	54500
Swirl number	0.47	0.49
Particle phase		
Particle mass flow rate (g/s)	0.34	1.0
Particle loading in the primary jet	0.034	0.17
Particle properties		
Particle mean number (μm)	45	
Particle material density (kg/m^3)	2500	
Stokesian particle response time (ms)	15.2	
Refractive index	1.52	

where U and W are the mean axial and tangential velocities and r is the radius. The values for the outer diameter of the inlet D_3 and the inner diameter of the test section D_5 are given in figure 1.

Furthermore, the particle mass flow rates and the properties of the glass beads are given in table 2. The particles have a smooth surface and are spherical in shape. Only less than about 2% of the number of particles are non-spherical or fragments [figure 3(b)], which results in small errors in sizing the beads. This particle material is ideal for PDA studies in particulate two-phase flows. The

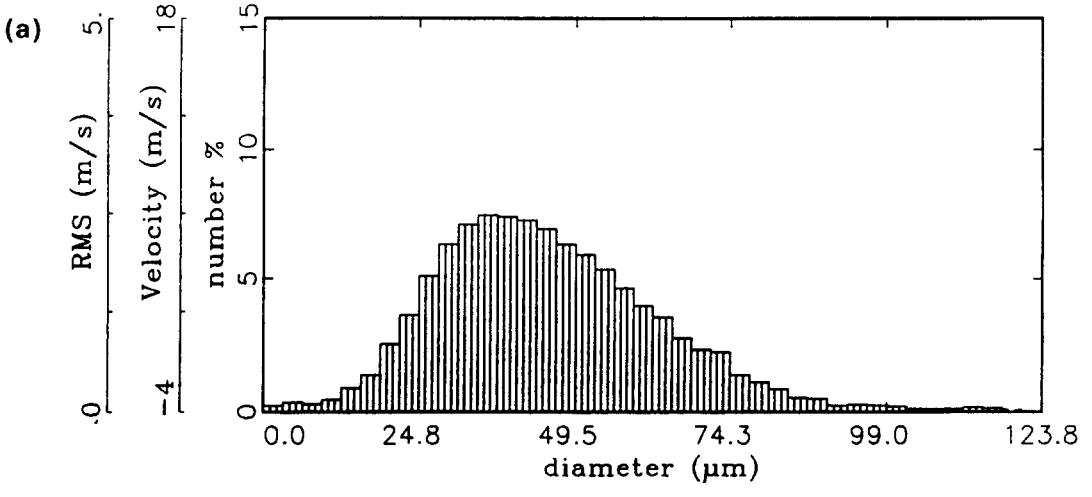

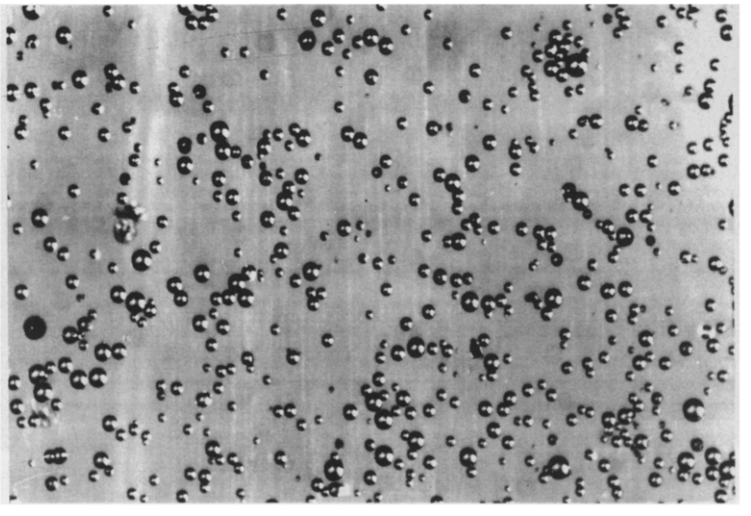

Figure 3. Dispersed-phase particles: (a) measured particle size distribution; (b) photograph of the glass beads.

particle size distribution obtained by a PDA measurement (18,000 samples) is given in figure 3(a). Since during the experiment some of the smaller particles were not collected in the cyclone separator but were cought in the paper filter, the particle material was frequently renewed in order to guarantee that the particles always have the same size distribution. This was ensured by measuring the particle size distribution at the inlet from time to time. The effects of particle damage could not be observed in the present measurements.

NUMERICAL METHOD

The particle-laden flow field was calculated using the Eulerian/Lagrangian approach for the gas and particle phases, respectively. The fluid flow calculations were based on the time-averaged Navier–Stokes equations in connection with the well-known k–ϵ turbulence model. More details about the numerical calculation of the fluid flow and the method of numerical solution can be found in Sommerfeld *et al.* (1992). The calculations were performed on a mesh of 80 × 75 control volumes in the streamwise and radial directions, respectively. The computational domain in the streamwise direction was extended up to 1.0 m downstream of the inlet and zero-gradient outflow conditions were applied.

The converged solution of the gas flow field was used for the simulations of the particle phase based on the Lagrangian approach, and a stochastic model for simulating the interaction of the particles with the fluid turbulence. For the calculation of the particle-phase mean properties, a large number of particles were traced through the flow field, typically more than 100,000 particles. The effect of the particle phase on the fluid flow was neglected in the present calculations, since only very small particle loadings were considered. The individual particle trajectories were obtained by solving the equations of motion for each particle in a cylindrical coordinate system where the added mass effect and the Basset history force were neglected, since the density ratio ρ_p/ρ is on the order of 2000. However, the lift force due to particle rotation (Rubinow & Keller 1961) was considered, since the particles acquire very high rotational velocities after a collision with the wall of the test section. The resulting equations for determining the change in particle location and the translational and rotational particle velocities are:

$$\frac{d\mathbf{X}_p}{dt} = \mathbf{U}_p, \qquad [3a]$$

$$m_p \frac{d\mathbf{U}_p}{dt} = \frac{\pi}{8}\rho D_p^2 c_d(\mathbf{U}-\mathbf{U}_p)|\mathbf{U}-\mathbf{U}_p| + \frac{\pi}{8}\rho D_p^3\{(\tfrac{1}{2}\nabla\times\mathbf{U})-\boldsymbol{\Omega}_p\}\times\{\mathbf{U}-\mathbf{U}_p\}+\mathbf{F} \qquad [3b]$$

and

$$I_p \frac{d\boldsymbol{\Omega}_p}{dt} = -\pi\mu D_p^3\{(\tfrac{1}{2}\nabla\times\mathbf{U})-\boldsymbol{\Omega}_p\}, \qquad [3c]$$

where $\mathbf{X}_p$, $\mathbf{U}_p$, $\boldsymbol{\Omega}_p$ and $\mathbf{U}$ are the particle position vector, the instantaneous velocity vectors of the particles' translational and rotational velocities and the instantaneous fluid velocity at the particle position. Furthermore, m_p is the particle mass and I_p is the moment of inertia for a sphere. The external forces $\mathbf{F}$ for the different velocity components are given as follows:

axial component $\mathbf{F}:=m_p g$;

radial component $\mathbf{F}:=m_p \dfrac{w_p^2}{r_p}$;

tangential component $\mathbf{F}:=m_p \dfrac{v_p w_p}{r_p}$.

The drag coefficient for a spherical particle is obtained in dependence of the particle Reynolds

number Re_p from

$$c_d = \begin{cases} \dfrac{24.0}{Re_p}(1.0 + \frac{1}{6}Re_p^{0.66}), & Re_p \leqslant 1000 \\ 0.44, & Re_p \geqslant 1000, \end{cases} \quad [4]$$

with

$$Re_p = \frac{D_p|\mathbf{U} - \mathbf{U}_p|}{\nu}. \quad [5]$$

The instantaneous fluid velocity in the above equations is randomly sampled from a Gaussian velocity distribution function which is characterized by the mean fluid velocity and the fluid r.m.s. value σ, which is evaluated from the turbulent kinetic energy by assuming isotropic turbulence:

$$\sigma = u_{rms} = v_{rms} = w_{rms} = \sqrt{\tfrac{2}{3}k}. \quad [6]$$

This instantaneous fluid velocity is assumed to influence the particle movement during a certain time period, the interaction time, before a new instantaneous velocity is sampled from the Gaussian distribution function. In this model, the successively sampled fluid velocity fluctuations are assumed to be uncorrelated. The interaction time of a particle with the individual eddies is limited by two criteria, namely the turbulent eddy lifetime and the time required for a particle to cross the eddy. As soon as the residence time of the particle within one eddy becomes larger than the eddy lifetime, a new velocity fluctuation is sampled from the local Gaussian velocity distribution associated with the particle position. The eddy lifetime or integral time scale of the most energetic eddies T_E can be estimated from the turbulent kinetic energy k and the dissipation rate ϵ as follows:

$$T_E = 0.3\frac{k}{\epsilon}. \quad [7]$$

The "crossing trajectory effect" is accounted for by integrating the distance travelled by the particle within one eddy and comparing it with the eddy length scale $L_E = T_E\sigma$. When the distance travelled by the particle within the considered eddy becomes larger than the eddy length scale, a new fluctuation velocity is assumed to act on the particle. The integration of the distance travelled by the particle within the eddy is performed by considering all three velocity components.

In order to account for the non-homogeneity of the turbulence along the particle trajectory, the eddy size and the time scale are updated according to the local turbulence properties as long as the particle is within the same eddy. Furthermore, the relative position of the particle within the eddy is corrected. This procedure is different from those described in previous publications (e.g. Gosman & Ioannides 1983), but was suggested previously by Milojevic (1990) in a similar form.

The above equations [3a–c] were solved by the Euler method, where the maximum allowable time step was set to be 10% of the minimum of the following characteristic time scales:

- The Stokesian response time of the particle.
- The time required for a particle to cross the mesh.
- The local eddy lifetime.

The boundary conditions for the particle tracking procedure were specified as follows. At the inlet, the particle velocities and the mass flux are specified according to the experimental conditions. Since there is no possibility of measuring particle rotational speeds, the result of a fully-developed pipe flow was used to specify the particle rotation at the inlet. A particle crossing the centreline is replaced by a particle entering at this location with opposite radial velocity.

The particle interaction with the solid wall was modelled as a three-dimensional inelastic collision process. For an inelastic collision process, one may identify a compression and a recovery period. The change in the particles' translational and rotational velocities during the bouncing process can be calculated from the impulse equations of classical mechanics. Two types of collisions may be distinguished—sliding and non-sliding collisions (Tsuji *et al.* 1985).

The type of collision is determined by the static coefficient of friction μ_0, the restitution ratio of the normal velocity components e and the velocity of the particle surface relative to the contact

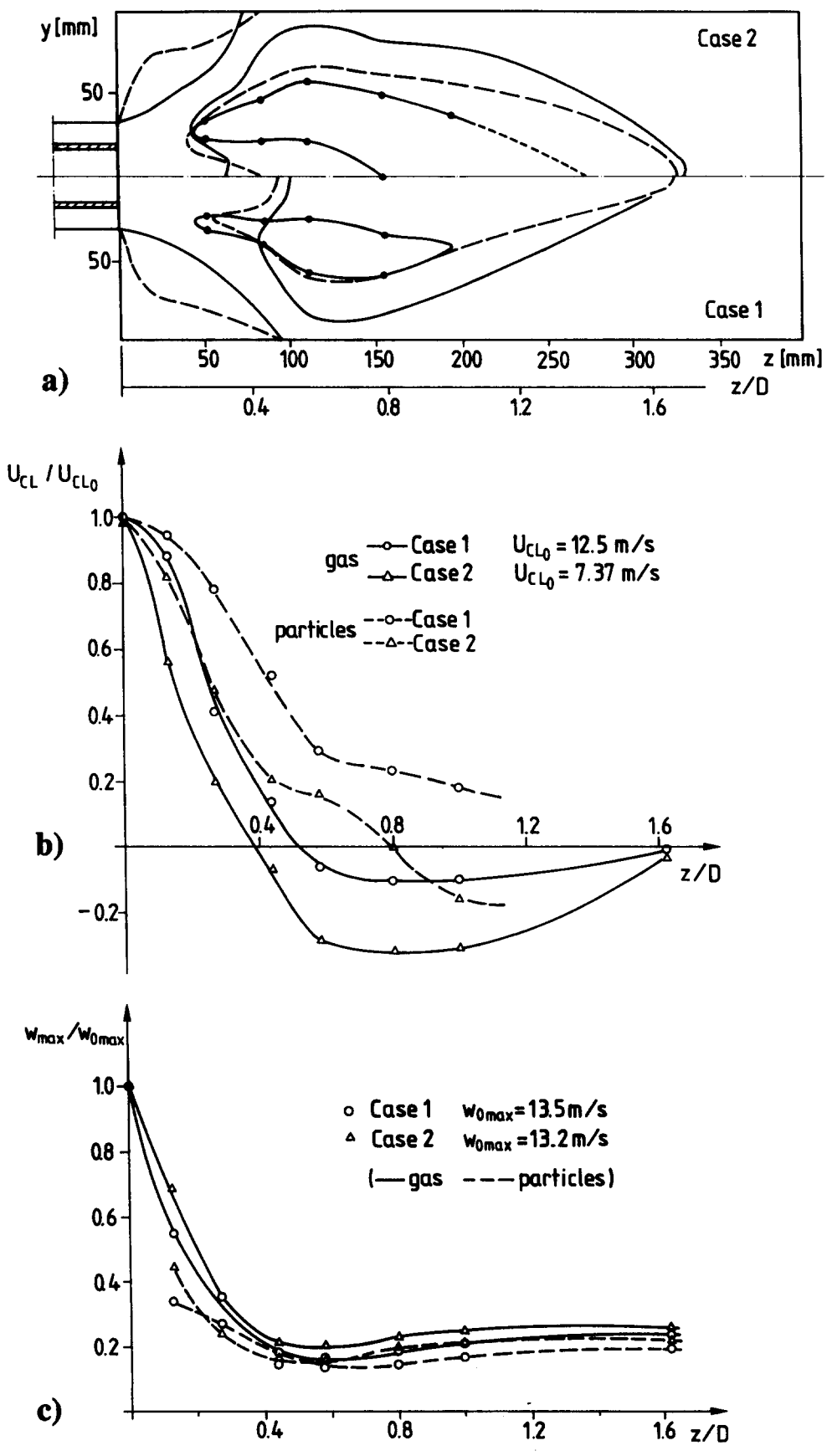

Figure 4. Velocity characteristics of the two considered swirl cases: (a) zero axial velocity lines for the gas (– – –) and particle phases (● – ●) and dividing streamlines (——); (b) axial gas (——) and particle velocities (– – –) along the centreline; (c) maximum tangential velocities for the gas (——) and particle phases (– – –).

point V_{R1}. A *non-sliding collision* takes place when the following condition is valid:

$$|V_{R1}| \leqslant \frac{7}{2}\mu_0(1+e)v_{p1},$$

$$V_{R1} = \sqrt{\left(u_{p1} - \frac{D_p}{2}\omega_{p1}^z\right)^2 + \left(u_{p1} + \frac{D_p}{2}\omega_{p1}^x\right)^2}; \quad [8]$$

where u_p, v_p and w_p are the translational velocity components and ω_p^x, ω_p^y and ω_p^z are the rotational velocity components of the particle in a cylindrical coordinate system. The subscripts 1 and 2 refer to the conditions before and after collision, respectively. For a *non-sliding collision*, the change in particle velocities is obtained by:

$$u_{p2} = \frac{5}{7}\left(u_{p1} + \frac{D_p}{5}\omega_{p1}^z\right), \quad \omega_{p2}^x = -\frac{2w_{p2}}{D_p},$$

$$v_{p2} = -ev_{p1}, \quad \omega_{p2}^y = \omega_{p1}^y,$$

$$w_{p2} = \frac{5}{7}\left(w_{p1} - \frac{D_p}{5}\omega_{p1}^x\right), \quad \omega_{p2}^z = \frac{2u_{p2}}{D_p}. \quad [9]$$

A *sliding collision* occurs when

$$|V_{R1}| > \tfrac{7}{2}\mu_0(1+e)v_{p1}. \quad [10]$$

The change in translational and rotational velocities throughout a *sliding collision* is obtained by:

$$u_{p2} = u_{p1} - \mu_d(1+e)v_{p1}\epsilon_x, \quad \omega_{p2}^x = \omega_{p1}^x - 5\mu_d(1+e)\frac{v_{p1}}{D_p}\epsilon_z,$$

$$v_{p2} = -v_{p1}, \quad \omega_{p2}^y = \omega_{p1}^y,$$

$$w_{p2} = w_{p1} - \mu_d(1+e)v_{p1}\epsilon_z, \quad \omega_{p2}^z = \omega_{p1}^z + 5\mu_d(1+e)\frac{v_{p1}}{D_p}\epsilon_x. \quad [11]$$

In these equations, ϵ_x and ϵ_z define the direction of motion of the particle contact point relative to the wall surface:

$$\epsilon_x = \frac{u_{p1} - \frac{D_p}{2}\omega_{p1}^z}{V_{R1}}; \quad \epsilon_z = \frac{u_{p1} + \frac{D_p}{2}\omega_{p1}^x}{V_{R1}}. \quad [12]$$

Throughout the paper the following constants are used in the wall collision model unless stated otherwise: $e = 0.8$, $\mu_0 = \mu_d = 0.3$.

In order to take into account the effect of the wide size spectrum of the particles used in the experiments on the particle mean velocities, the velocity fluctuations and the dispersion process, the numerical calculations were performed considering the particle size distribution shown in figure 3(a). The procedure for simulating the particle size distribution by a log-normal distribution function was described by Sommerfeld (1990).

FLOW CHARACTERISTICS AND CENTRELINE PROPERTIES

The swirling flow established in the experiments exhibits a closed central recirculation bubble just downstream of the inlet and a rather short recirculation at the edge of the pipe expansion. Due to the strong spreading of the swirling jet, the reattachment length is considerably shorter than that for a similar pipe expansion flow without swirl (Sommerfeld *et al.* 1991).

An overview of the gas flow field and the particle behaviour in the two swirl flow conditions (cases 1 and 2) considered is given in figure 4(a), where the gas-phase zero axial velocity lines, the dividing streamlines and the zero axial velocity lines for the particles (averaged over all particle classes) are shown. The width of the central recirculation bubble is almost identical for both cases, whereas the length is larger for case 2. As a result of the lower axial momentum of the primary jet in case 2, the recirculation bubble moves closer to the inlet. The slightly higher swirl number

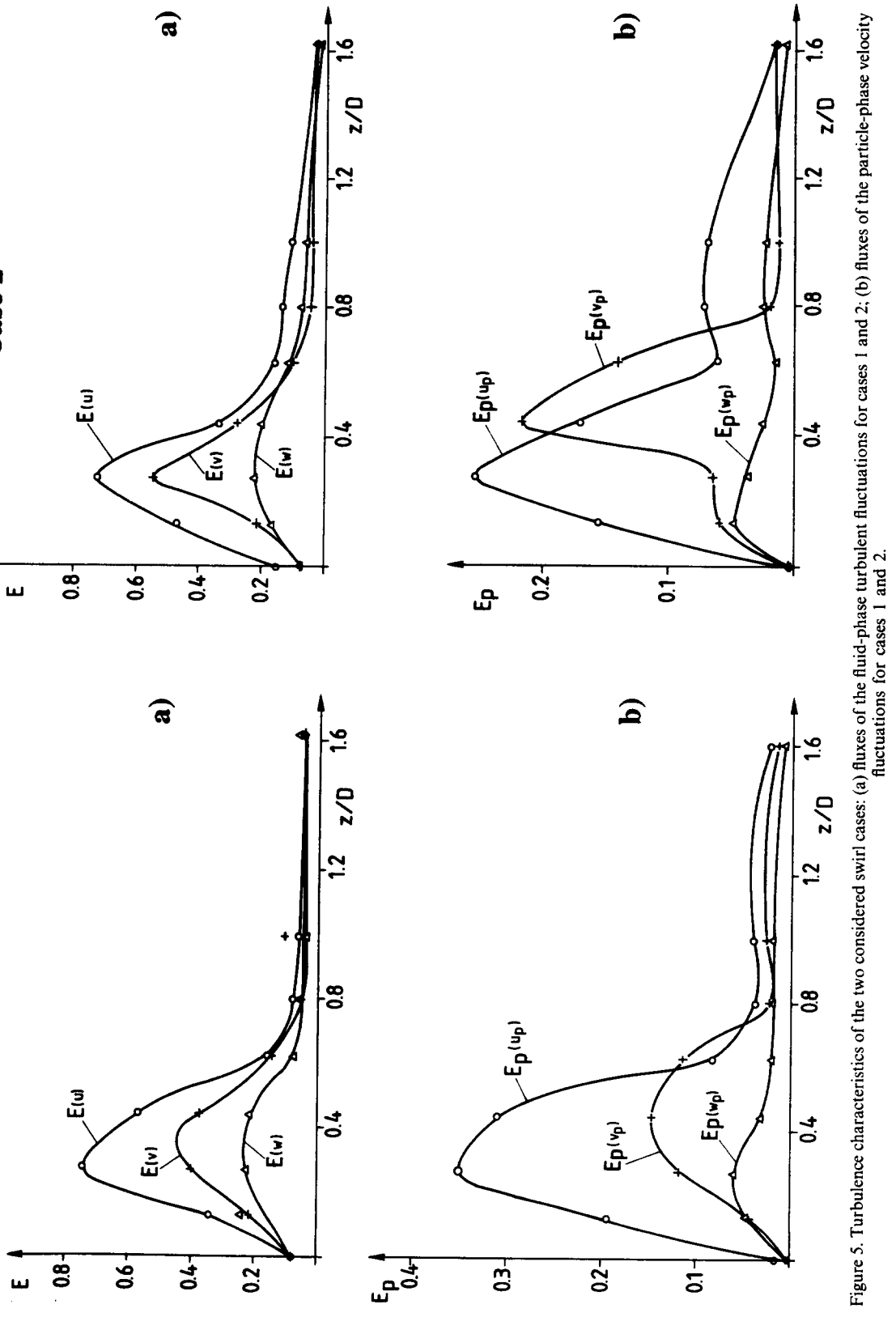

Figure 5. Turbulence characteristics of the two considered swirl cases: (a) fluxes of the fluid-phase turbulent fluctuations for cases 1 and 2; (b) fluxes of the particle-phase velocity fluctuations for cases 1 and 2.

in this case also gives rise to a shorter reattachment length of the recirculation region at the edge of the pipe expansion, as compared with case 1.

The area of negative axial particle velocity exhibits an annular shape ranging from about 50 to 200 mm downstream of the inlet for swirl case 1. In case 2, where the particle initial momentum is lower, the particles have longer residence times in the flow and, therefore, respond faster to the flow reversal in the central recirculation bubble. The resulting area of negative particle axial velocities becomes wider and extends from 50 to about 250 mm in the streamwise direction.

The development of the axial gas velocity along the centreline [figure 4(b)] shows that the magnitude of the negative velocity established in case 2 is considerably higher than that in case 1. This also results in a much faster deceleration of the particles at the centreline for case 2, and they attain negative axial mean velocities at 155 mm downstream of the inlet. The plotted axial particle velocity is again the average of all particles in the size spectrum. An interesting effect is the rather sudden change of the slope in the centreline particle velocity at certain locations for both cases. For case 1, this occurs at $z = 112$ mm where the particles begin to decelerate at a slower rate. The axial particle velocity in case 2 has two distinct changes: from $z = 85$ mm, the particles begin to decelerate at a slower rate; and from $z = 112$ mm again at a higher rate. This phenomenon is related to the particle separation effects occurring in swirling flows, which results in a considerable increase in the particle mean number diameter along the centreline, and it will be explained in more detail in the following paragraphs.

The streamwise development of the maximum tangential velocity measured at each cross-section for the gas and particle phases is shown in figure 4(c). The difference between the two swirl cases considered is rather small for the maximum gas and particle tangential velocities. The particles lag behind the air flow throughout the flow field.

The overall turbulence characteristics and anisotropy of the flow turbulence may be characterized by calculating the fluxes of the normal Reynolds stresses (Weber *et al.* 1990) which were measured at the different cross-sections. These fluxes of turbulence are obtained by integrating each cross-sectional profile according to the equation

$$E(\sigma_i) = 2\pi\rho \int_0^R \frac{\overline{\sigma_i^2}}{2} Ur \, \mathrm{d}r, \qquad [13]$$

where σ_i represents the three measured normal Reynolds stresses u_{rms}, v_{rms} and w_{rms}, whereby the turbulent fluxes of each velocity component are calculated. The calculated fluxes show the turbulence intensities of the three components and yield information about the anisotropy in the normal Reynolds stresses. The highest turbulence intensities with strong anisotropy were found in the mixing region between the primary and secondary jets just upstream of the central recirculation bubble for both case 1 and case 2 [figure 5(a)]. The maxima in the turbulent fluxes of all three components were found at about 50 mm downstream of the inlet, where the values for the tangential component are lowest. Further downstream, the turbulence intensity decreased, and the turbulent fluxes of the three normal Reynolds stresses approached similar values within the recirculation bubble.

The velocity fluctuations of the particle phase may be characterized in a similar way by calculating the fluxes of the velocity fluctuations $\sigma_{\mathrm{p}i}$ in the three directions:

$$E_{\mathrm{p}}(\sigma_{\mathrm{p}i}) = 2\pi\rho \int_0^R \frac{\overline{\sigma_{\mathrm{p}i}^2}}{2} Ur \, \mathrm{d}r. \qquad [14]$$

Since the particles are not able to follow the turbulent velocity fluctuations of the air flow in most parts of the flow, the integrated fluxes of the particles' velocity fluctuations are lower than those of the gas phase for both swirl conditions. The location of the flux maximum for the streamwise velocity fluctuations of the particles is identical to that of the air flow [figure 5(b)]. For the fluxes of the particles' radial velocity fluctuation, the maximum is shifted towards the beginning of the central recirculation bubble which indicates a strong radial transport of the particles in this region of flow reversal. Especially in case 2, the velocity fluctuations of the particle phase in the radial direction become larger than the streamwise fluctuations.

PARTICLE RESPONSE CHARACTERISTICS

The behaviour of the differently sized particles in swirling flows may be characterized by introducing two time-scale ratios for the different flow regimes, which depend on the particle response in these regions. The first time-scale ratio describes the particle response in the region from the primary inlet to the stagnation point at the top of the central recirculation bubble, and is defined as the ratio of the particle response time τ_{p1} and the time the particles need to reach the stagnation point τ_s, which is the so-called Stokes number:

$$S_1 = \frac{\tau_{p1}}{\tau_s}. \qquad [15]$$

Here, τ_s is obtained from the distance between the primary jet exit and stagnation point Δx_s and the gas velocity at the centreline of the primary jet U_{p0}:

$$\tau_s = \frac{\Delta x_s}{U_{p0}} \qquad [16]$$

The particle response times, based on the modified Stokesian drag, for the two regions are defined as

$$\tau_{p1,2} = \frac{D_p^2\left(1 + 2\frac{\rho_p}{\rho}\right)}{36\nu f_{d1,2}}, \qquad [17]$$

with

$$f_{d1,2} = 1.0 + \tfrac{1}{6}\,\mathrm{Re}_{p1,2}^{0.66}, \quad \mathrm{Re}_{p1} = \frac{D_p|U_{p0} - U_{f0}|}{\nu}, \quad \mathrm{Re}_{p2} = \frac{D_p|U_{ps} - U_{f\min}|}{\nu}.$$

Furthermore, D_p, ρ_p, ρ and m are the particle diameter, particle material density, fluid density and fluid kinematic viscosity, respectively. The relative velocities between the gas and particle phases, used for the calculation of the Reynolds number, are those at the inlet and the stagnation point of the central recirculation bubble.

The particle response to the flow reversal within the central recirculation bubble may be characterized by defining a time-scale ratio of the time t_{p0} which the particle needs to be decelerated to zero axial velocity and the time t_{int} in which the particle is able to interact with the recirculation

Table 3. Ratios of the characteristic time scales describing the particle response in a swirling flow with a central recirculation bubble (note that here τ_p is the particle response time based on Stokesian drag)

D_p (μm)	τ_p (ms)	Case 1[a]		Case 2[b]	
		S_1	S_2	S_1	S_2
20.0	3.004	0.463	0.004	0.605	0.002
30.0	6.758	1.024	0.049	1.359	0.021
40.0	12.015	1.790	0.151	2.413	0.061
50.0	18.773	2.756	0.295	3.764	0.116
60.0	27.033	3.916	0.472	5.412	0.183
70.0	36.795	5.263	0.678	7.356	0.261
80.0	48.059	6.793	0.910	9.596	0.349
90.0	60.825	8.501	1.165	12.129	0.447
100.0	75.092	10.383	1.443	14.957	0.553
110.0	90.862	12.435	1.742	18.077	0.667
120.0	108.133	14.654	2.061	21.489	0.790
130.0	126.906	17.035	2.400	25.192	0.920
140.0	147.181	19.577	2.758	29.186	1.058
150.0	168.958	22.276	3.134	33.470	1.204

[a]Other parameters: $\Delta x_s = 73$ mm, $L = 252$ mm, $U_{f0} = 12.5$ m/s, $U_{p0} = 12.0$ m/s, $U_{f\min} = -2.15$ m/s.
[b]Other parameters: $\Delta x_s = 36$ mm, $L = 300$ mm, $U_{f0} = 7.4$ m/s, $U_{p0} = 7.3$ m/s, $U_{f\min} = -3.46$ m/s.

(a)

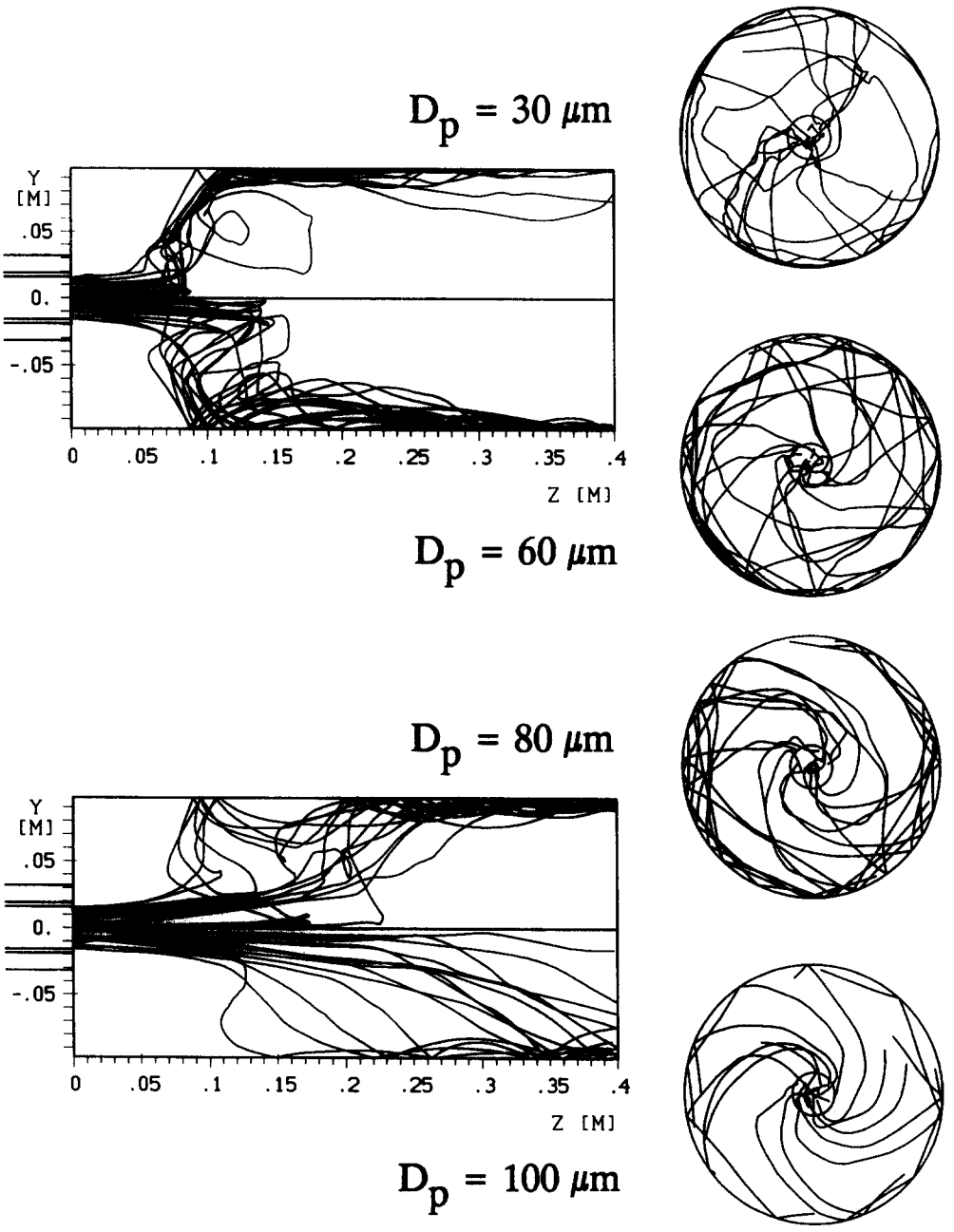

Fig. 6—*continued opposite.*

bubble:

$$S_2 = \frac{t_{p0}}{t_{int}}. \qquad [18]$$

The time t_{p0} is estimated by using the integrated form of the particles' equations of motion:

$$U_p = U_f - (U_f - U_p)\exp\left(-\frac{\Delta t}{\tau_p}\right) \qquad [19]$$

and

$$t_{p0} = \tau_{p2} \ln\left(\frac{U_{f\min} - U_{ps}}{U_{f\min}}\right), \qquad [20]$$

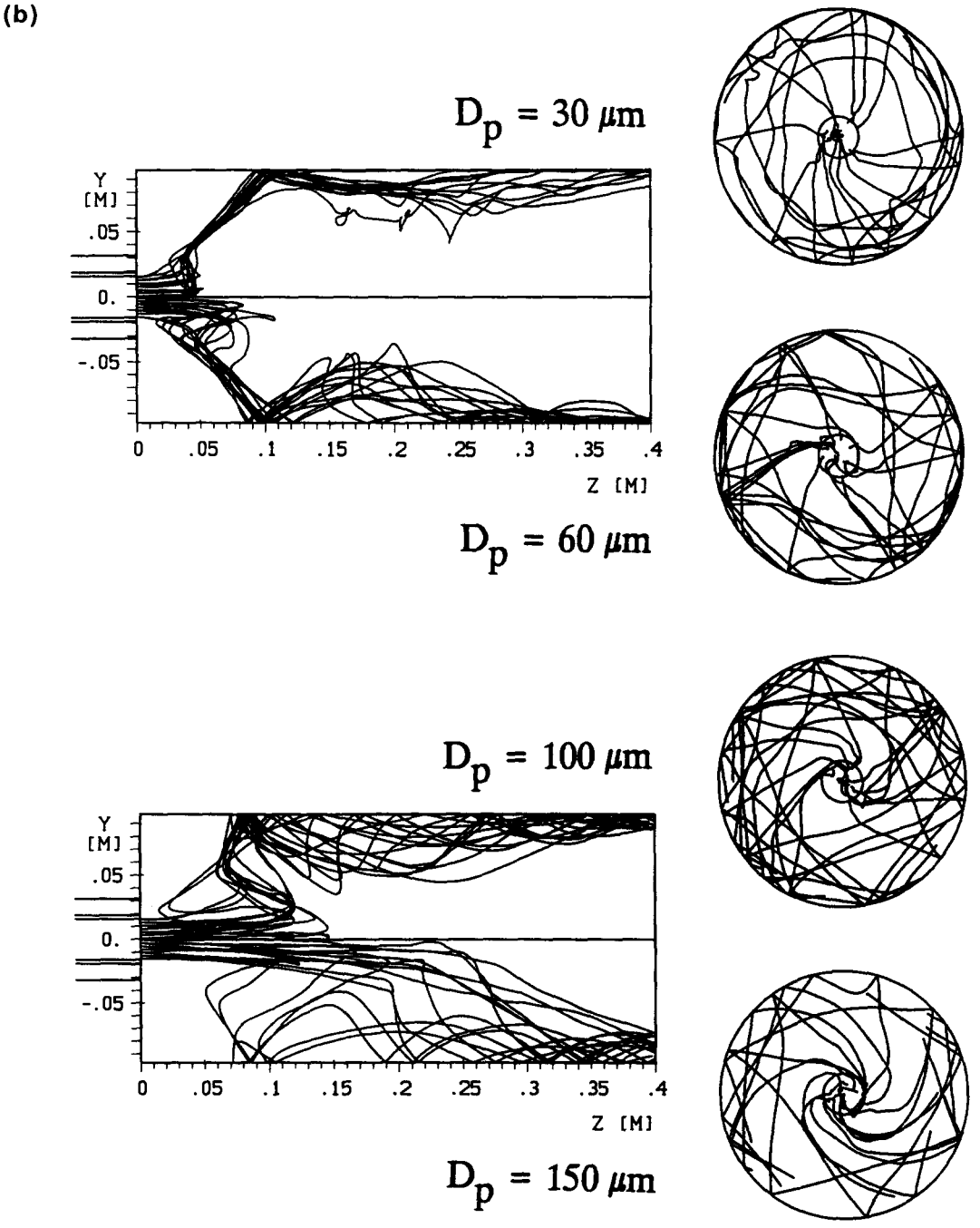

Figure 6. Numerically-simulated particle trajectories: (a) case 1; (b) case 2.

where U_{ps} is the particle velocity at the stagnation point of the recirculation bubble and $U_{f\min}$ is the lowest fluid velocity within the recirculation bubble on the centreline. The particle velocity at the stagnation point is obtained by solving [19] for the initial region from the inflow to the stagnation point:

$$U_{ps} = U_{p0} \exp\left(-\frac{1}{\tau_{pl}} \frac{\Delta x_s}{U_{p0}}\right); \qquad [21]$$

U_{p0} is the particle velocity at the inlet and Δx_s is the distance from the inlet to the stagnation point. The possible interaction time of the particle with the reverse flow region t_{int} is calculated from the

streamwise extension of the recirculation bubble L and the average particle velocity $U_{p\,av}$ in this region:

$$t_{int} = \frac{L}{U_{p\,av}}, \qquad [22]$$

with

$$U_{p\,av} = \frac{\int_0^{t_{p0}} U_p \, dt}{t_{p0}}. \qquad [23]$$

The results of the calculated time-scale ratios S_1 and S_2 for the two considered flow configurations and for different particle diameters are summarized in table 3 together with the input data from the numerical calculations.

In the initial region from the inlet to the stagnation point of the central recirculation bubble, only particles up to approx. 20 μm are able to follow the flow for both swirl cases, and the time-scale ratio S_1 is <1. For swirl case 1, the time-scale ratio S_2 for particles up to 80 μm is <1, which indicates that they are able to respond to the flow reversal. Numerically-simulated particle trajectories show that particles up to about 80 μm are decelerated to zero axial velocity within the central reverse flow region and then begin to move towards the inlet while they are centrifuged out of the core region [figure 6(a)]. Larger particles traverse the complete recirculation bubble due to their higher inertia.

In swirl case 2, the time-scale ratio S_2 is <1 for particles up to about 130 μm. Due to the lower particle velocity at the inlet for this case, the particles are decelerated to zero axial velocity already within the initial part of the recirculation bubble [figure 6(b)]. While the particles move towards the inlet, they are radially transported outward and entrained into the annular swirling air stream. Then, the particles begin to move downstream again, still being moved outward before they collide with the wall of the test section. The larger particles (i.e. >60 μm) begin to bounce along the wall and, finally, all of the particles accumulate near the wall. The rebound heights become larger with increasing particle diameter, and the cross-sectional views of the particle trajectories show that the larger particles pass through the outer parts of the central recirculation bubble after they have

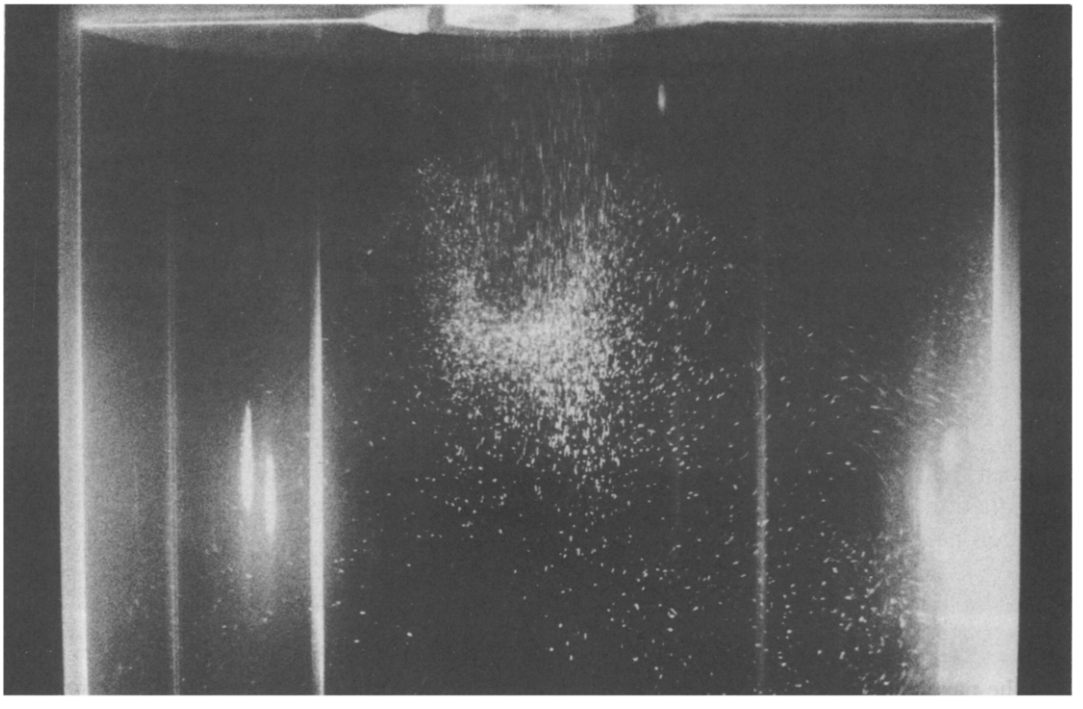

Figure 7. Flow visualization of the particle motion.

rebounded from the wall for the first time. The small particles, on the other hand, follow the rotational motion of the flow (figure 6).

The shape of the particle trajectories in the initial part of the recirculation bubble also explains the annular shape of the particle recirculation region, which has already developed just downstream of the inlet. This behaviour of the particles was also observed in the experiments by means of flow visualization, applying the laser light sheet method (figure 7). It is clearly seen that the particles penetrate into the recirculation bubble, are decelerated and then begin to move upward before they are entrained into the flow coming from the secondary inlet.

Furthermore, the numerical calculations allow the determination of the most important parameters for combustion systems, namely the particle residence time in certain flow regions. Especially in the central recirculation bubble where the combustion takes place, knowledge of the correlation between particle size and residence time can support the layout of a swirl burner. For the case considered with a low particle injection velocity, it was found that the residence time of large particles can be increased considerably compared to the case with a high injection velocity (figure 8). This effect would support the complete burnout of the large particles. For the case with a high particle injection velocity, a maximum in the residence time was found for the 70 μm

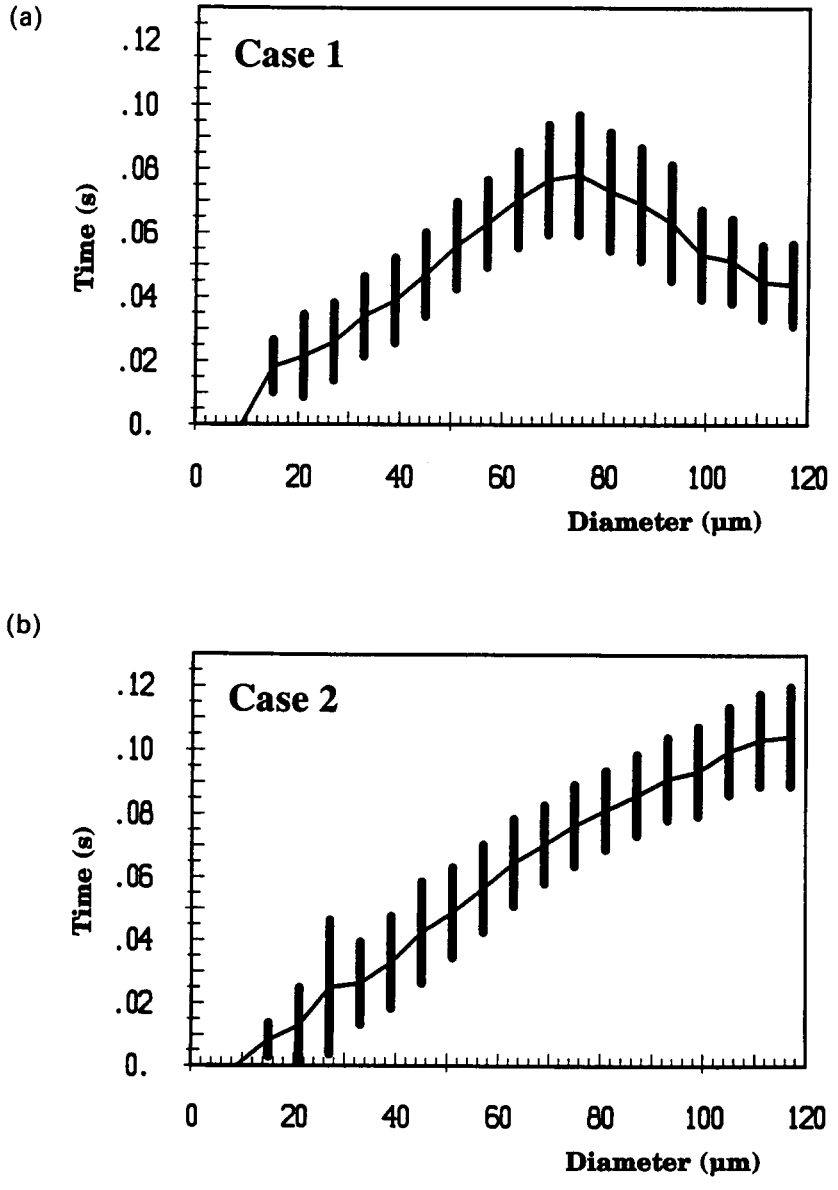

Figure 8. Correlation between particle size and residence time: (a) case 1; (b) case 2.

particles, while for the case 2, the maximum is reached for 120 μm particles. It is important to note, however, that the residence time for small particles (i.e. $<70\,\mu$m) is not considerably different for the two cases.

MEASURED RADIAL PROFILES

The measurements of the cross-sectional profiles for the mean gas and particle velocities, the velocity fluctuations and the development of the particle mass flux and the particle mean diameter reveal the particle response and dispersion characteristics described in the last section. The measurements of the particle mass flux for the two flow situations already show considerable differences (figure 9). The maximum of the mass flux near the centreline remains up to 200 mm downstream of the inlet for case 1. While in case 2, the particles begin to accumulate near the wall quite early (from $z = 112$ mm), and the maximum of the mass flux appears near the centreline only up to about $z = 112$ mm. Furthermore, it may be seen that the recirculating particle mass (i.e. negative mass flux) is considerably higher for swirl case 2. In addition, the fraction of recirculating particles is found to be higher in the initial part of the recirculation bubble for this case. This indicates that this flow condition is more suitable for pulverized coal combustion when the diameter of the coal particles is rather large and where the devolatilization occurs in the central recirculation bubble (Smart & Weber 1989). This effect may considerably reduce NO_x formation.

Due to the different responses of the differently sized particles to the flow reversal, the flow turbulence and to the centrifugal effects, a considerable separation of the particle phase is observed in the two flow conditions considered. These effects result in a considerable change in the particle size distribution and, hence, in the particle mean diameter throughout the flow field. Due to the higher inertia of the larger particles, they remain concentrated in the core region while the smaller ones are entrained into the flow coming from the annulus. This results in a continuously increasing number mean particle diameter in the streamwise direction in the core region of the flow for both cases (figure 10). As already demonstrated by the numerically-simulated particle trajectories, the particles have more time to respond to the flow reversal and the centrifugal forces in case 2, due to their lower initial velocity. Hence, a minimum in the particle mean diameter is already observed in the core region of the central recirculation region at $z = 195$ mm, which implies that the majority of larger particles have also been transported towards the wall. Since the particle mass flux is already very low at this location, only some smaller recirculating particles, or those which have been reflected from the wall, were recorded here.

These effects also explain the considerable changes in the streamwise component of the particle velocity near the centreline, which is shown in figure 4. In case 1, the particle mean diameter increases considerably downstream of $z = 112$ mm, which results in a decrease in the particle axial velocity at a slower rate (i.e. higher probability of slower large particles). For case 2, a remarkable increase in the particle mean diameter is already observed at $z = 85$ mm and, hence, the particle velocity in the streamwise direction decreases at a slower rate. Further downstream ($z = 195$ mm), the average axial particle velocity begins to decrease again at a faster rate, since only small particles are present here. In conclusion, it should be mentioned that the development of the particle mean diameter is a very sensitive parameter with regard to the quality and symmetry of the flow, which is very good for both conditions.

In order to demonstrate the particle velocity characteristics in the two flow conditions considered, the measured radial profiles of the axial mean velocity and the corresponding velocity fluctuations for both cases are shown in figures 11 and 12 for the gas phase and the three particle size classes (i.e. 30, 45 and 60 μm). These results again demonstrate the behaviour of particles with different diameters, which is strongly governed by inertial effects in this complex flow. The particles are not able to follow the rapid expansion of the air jets and the resulting deceleration of the flow. Hence, the particles maintain a higher velocity than the air flow in the core region of the test section and within the central recirculation bubble. The larger particles (i.e. 60 μm) have the highest velocities due to their larger inertia. In swirl case 2, it was observed that within the circulation bubble, the particles acquire higher negative axial velocities than in case 1.

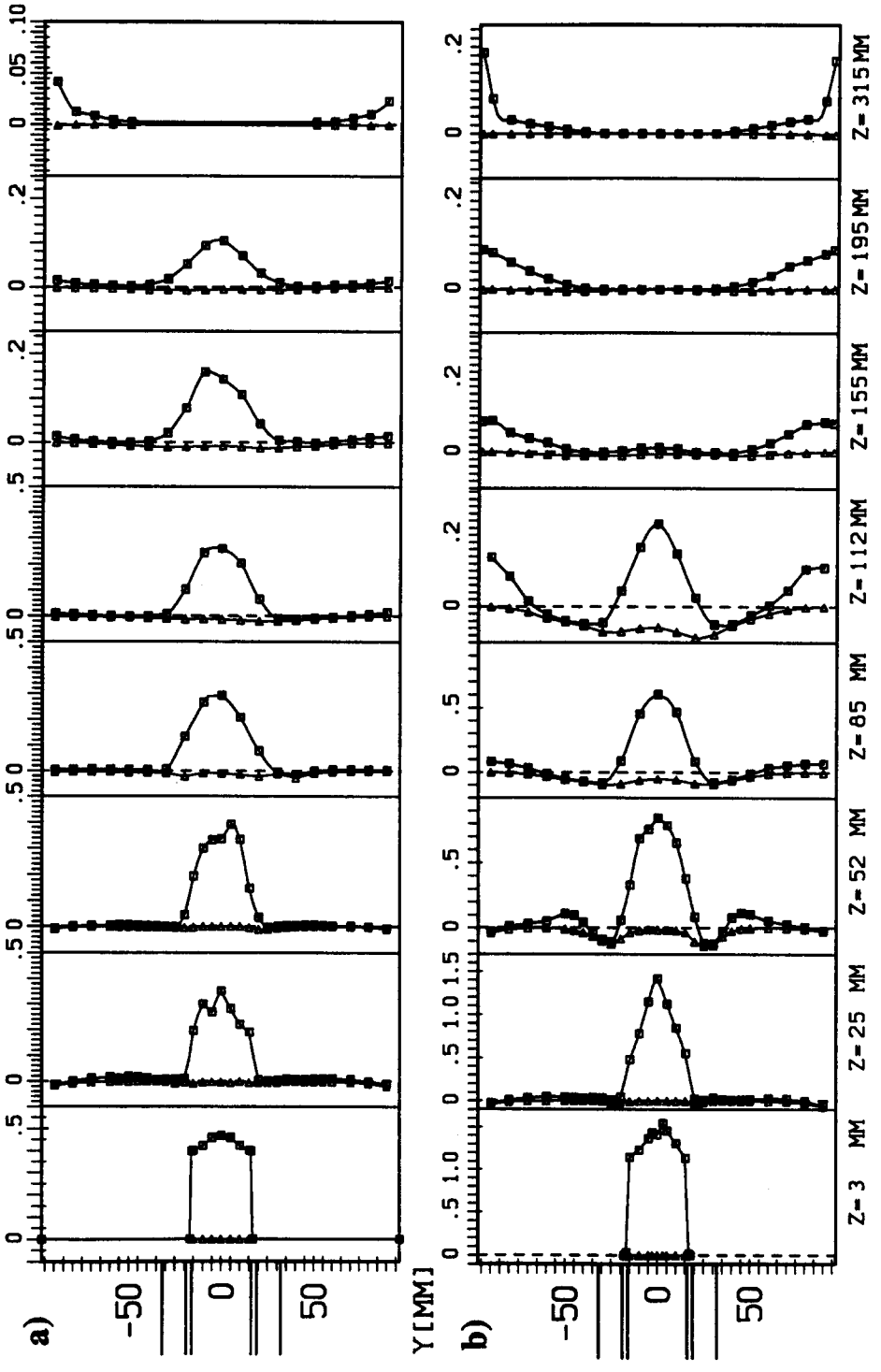

Figure 9. Measured particle mass flux profiles [kg/m^2 s] (□, total axal mass flux; △, negative axial mass flux): (a) case 1; (b) case 2.

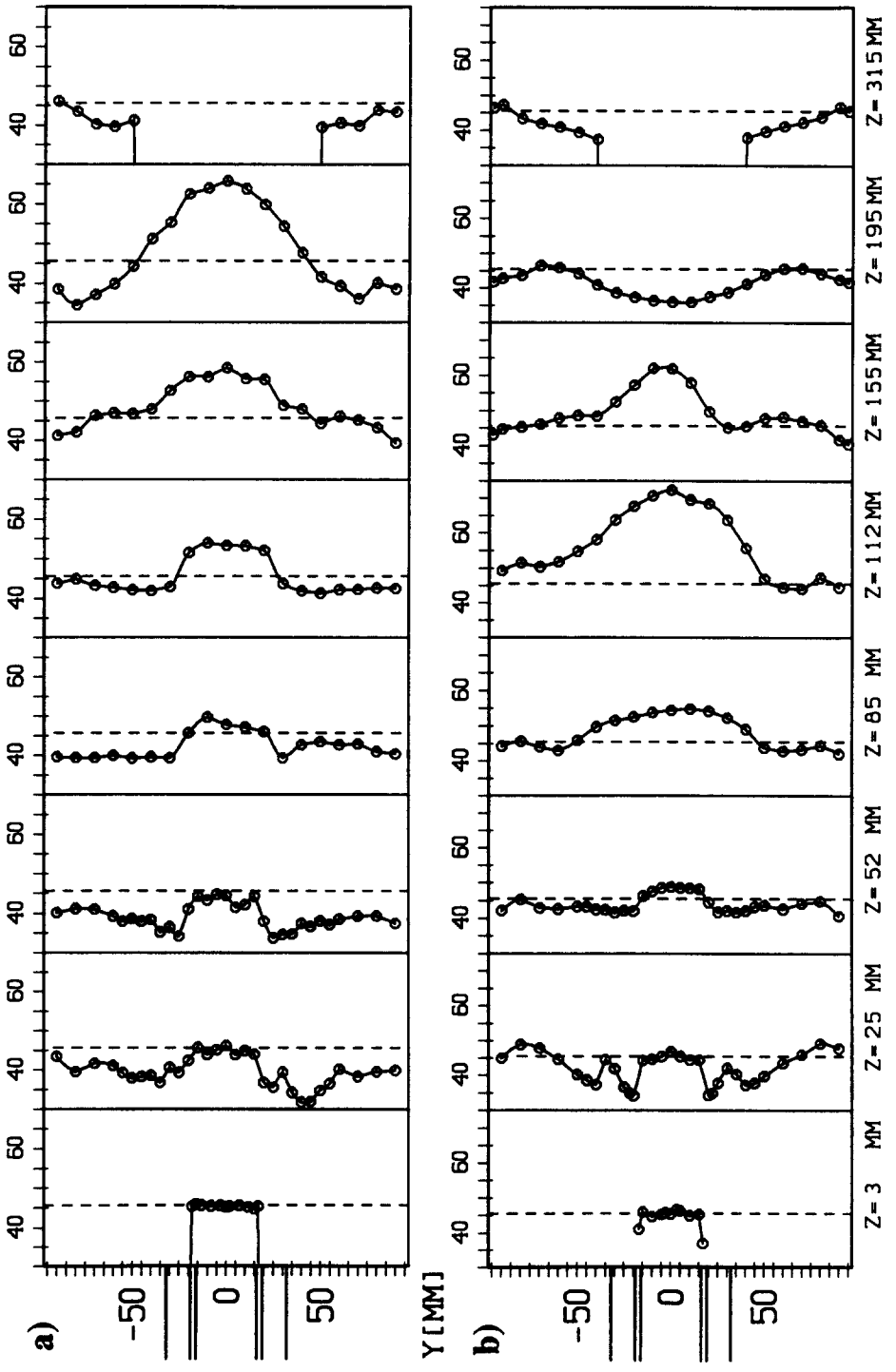

Figure 10. Measured development of particle mean diameter (μm): (a) case 1; (b) case 2.

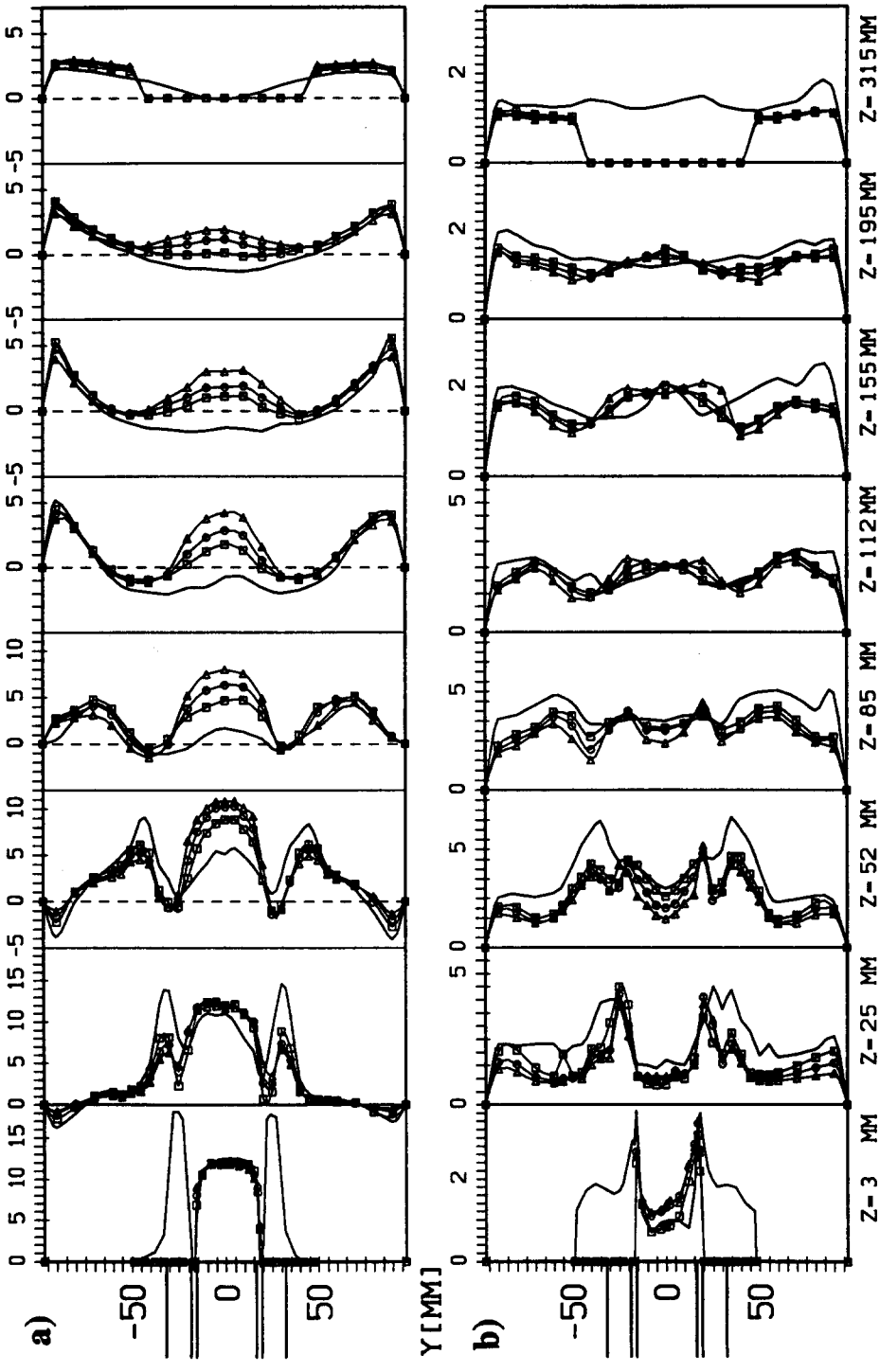

Figure 11. Profiles of axial mean velocities (a) and r.m.s. values (b) for air and particles for case 1 in (m/s): ——, air; □, 30 μm particles; ○, 45 μm particles; △, 60 μm particles.

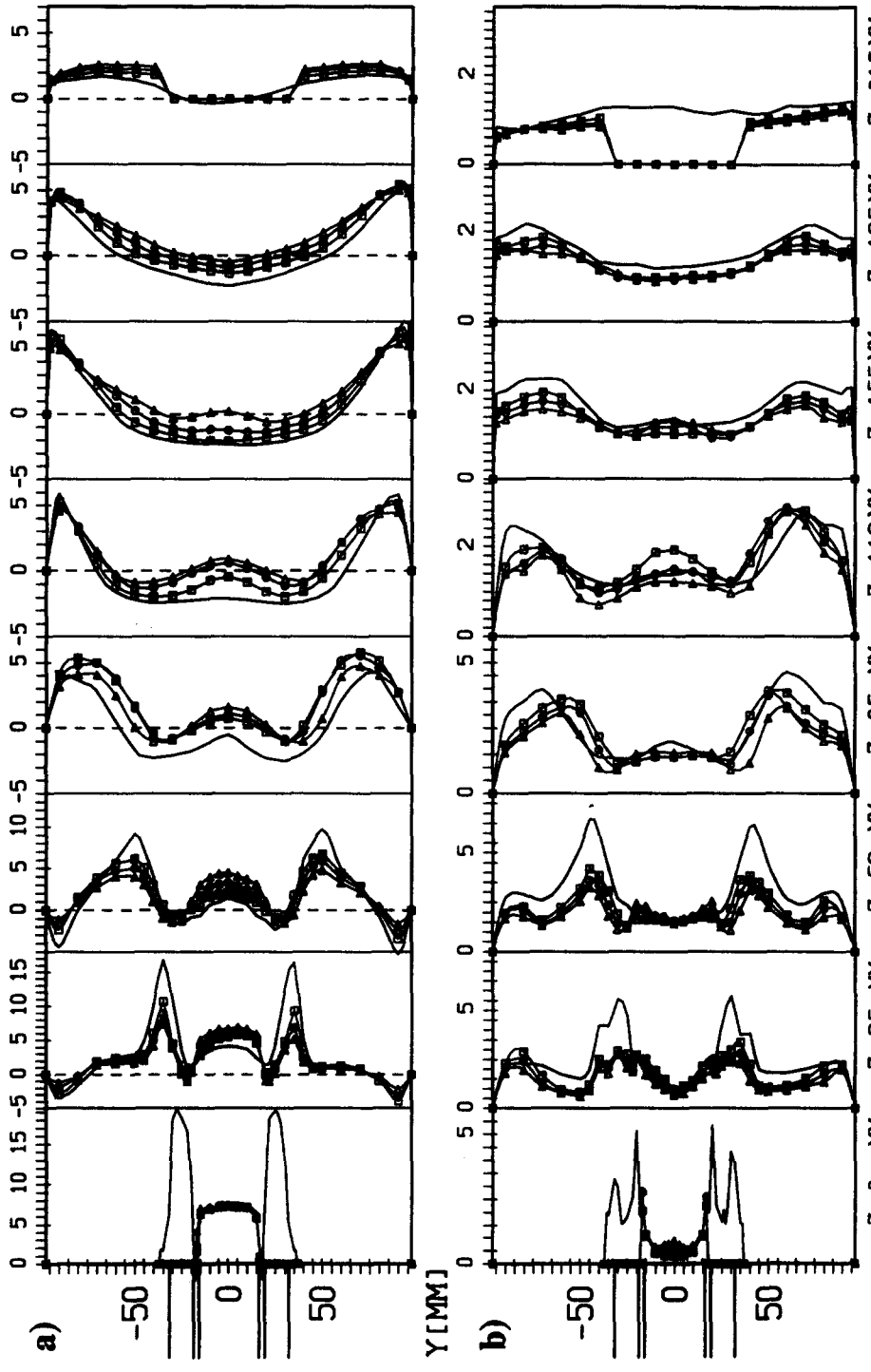

Figure 12. Profiles of axial mean velocities (a) and r.m.s. values (b) for air and particles for case 2 in (m/s): ——, air; □, 30 μm particles; ○, 45 μm particles; △, 60 μm particles.

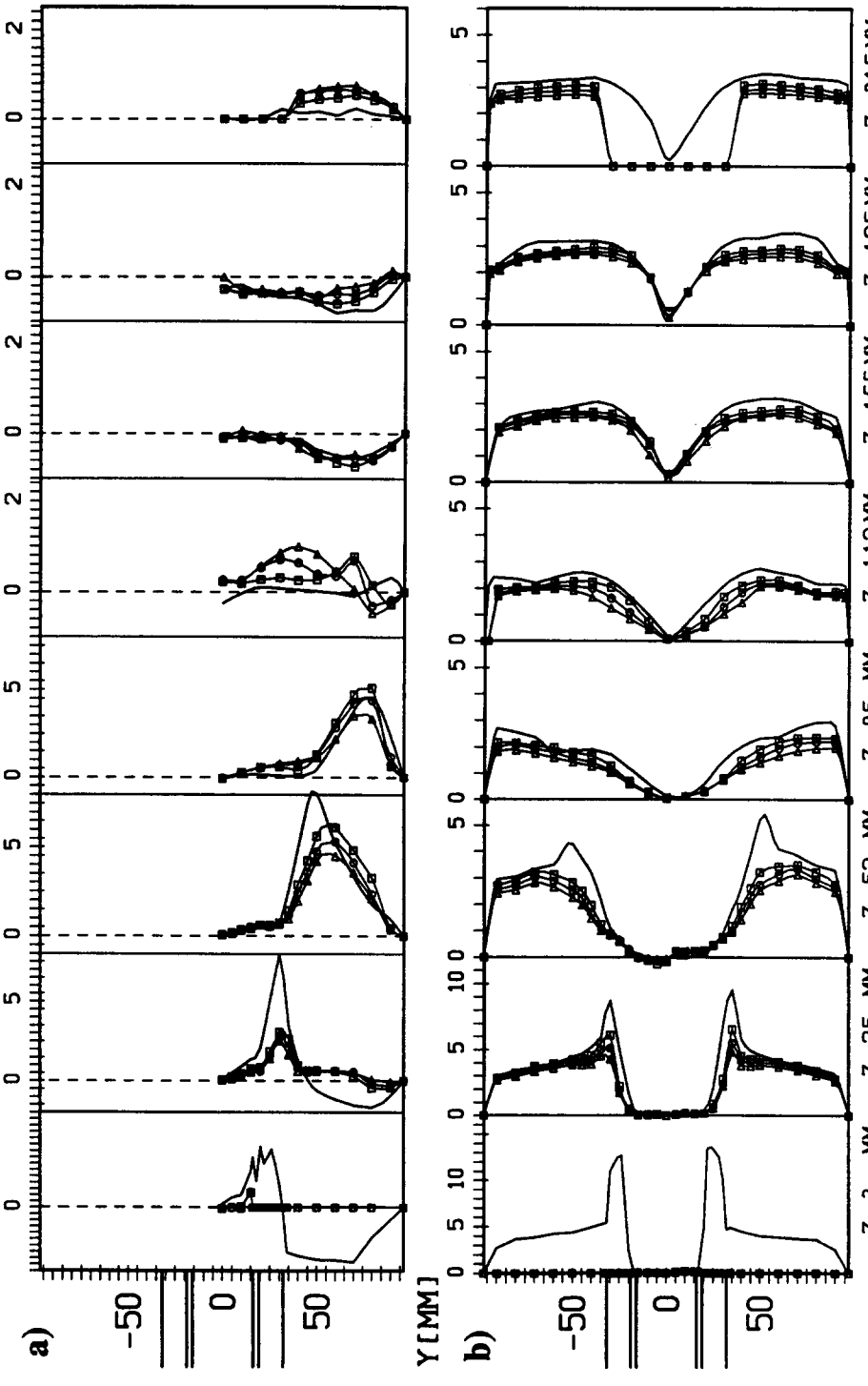

Figure 13. Profiles of radial mean velocity (a) and tangential mean velocity (b) for case 2 in (m/s): ——, air; □, 30 μm particles; ○, 45 μm particles; △, 60 μm particles.

An interesting phenomenon was observed for the velocity fluctuations of the particles in the streamwise direction (figures 11 and 12). For both cases one finds regions where the r.m.s. value is higher for the particles than for the gas phase. This, of course, cannot result from the response of the particles to the fluid turbulence. This effect is a consequence of the so-called "history effect" (Sommerfeld & Qiu 1991) and is caused by the fact that particles from completely different directions cross a certain location within the recirculation bubble and near its edge. This means that both particles issuing straight from the inlet, which still have positive velocities, and recirculating particles, which come from further downstream, are sampled at these locations. Therefore, this effect results in broader velocity distributions for the particles compared to the gas velocity distribution. Especially in case 1, this effect is more pronounced for the larger particles. Furthermore, it is obvious that in certain regions the velocity fluctuations of the larger particles are higher than for the smaller ones (e.g. case 1 at $z = 112$ and 155 m, case 2 at $z = 52$ and 85 mm), which is again a result of inertial effects.

The radial and tangential mean velocity profiles for the gas phase and the three classes of particles are shown in figure 13 for case 2. The radial velocity profiles [figure 13(a)] could only be measured for half a cross-section due to limited optical access. Due to the rapid expansion of the jets, the gas and particles move radially outward up to approx. $z = 85$ mm. As a result of their inertia, the particles have slightly higher radial mean velocities than the gas phase. From $z = 112$ downstream

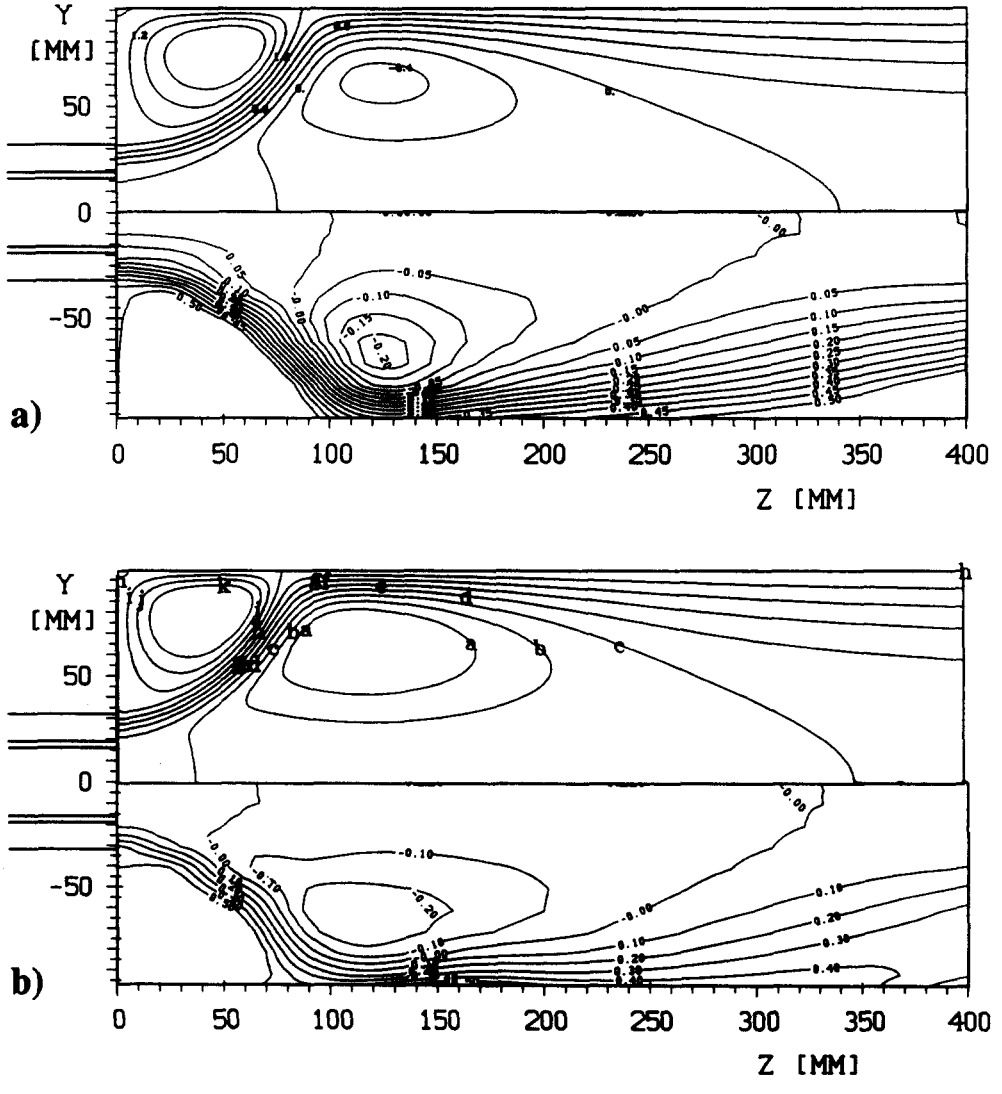

Figure 14. Measured and calculated gas-phase streamlines (the upper and lower half of each figure correspond to the calculations and measurements, respectively): (a) case 1; (b) case 2.

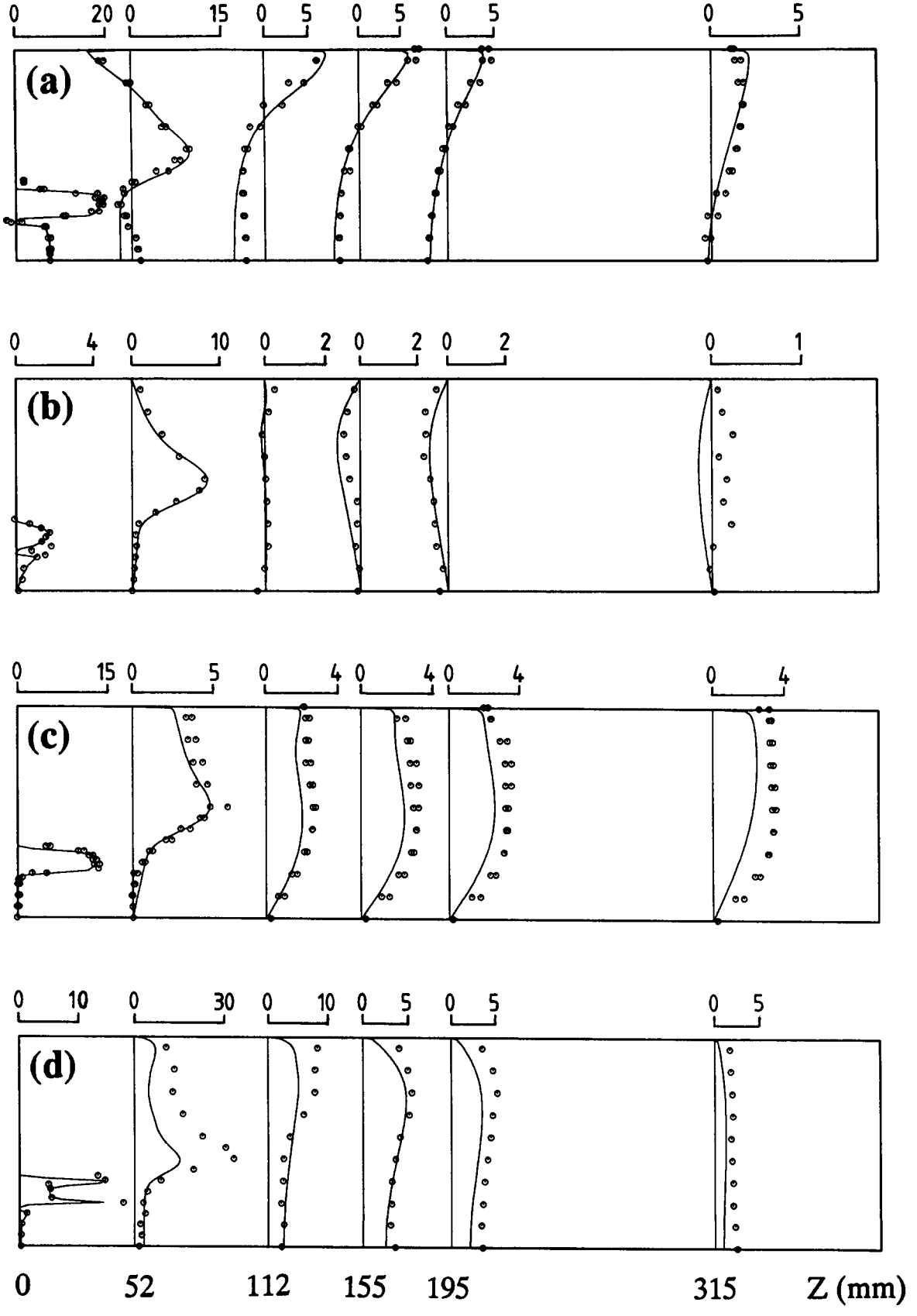

Figure 15. Comparison between measurements and predictions (gas phase, case 2): (a) axial mean velocity; (b) radial mean velocity; (c) tangential mean velocity; (d) turbulent kinetic energy.

of the inlet the particles move inward, since they have rebounded from the wall [see also figure 6(b)].

The tangential velocity profiles of the gas and particles [figure 13(b)] demonstrate that the particles lag behind the rotation of the gas flow. From the beginning of the central recirculation bubble at typical vortex structure may be identified where, in the core region, a solid body rotation develops for the gas and particle phases.

COMPARISON BETWEEN EXPERIMENTS AND CALCULATIONS

Although the standard k–ϵ model has been applied for calculating the fluid flow, a rather good agreement between the experiments and predictions was obtained for the gas and particle phases. The comparison of the calculated streamlines of the gas flow with those obtained from the integration of the measured axial velocity shows that the flow field is predicted reasonably well for both conditions (figure 14). The most obvious difference is that the axial extension of the central recirculation bubble is predicted to be larger at the top and downstream ends for both cases. The predicted width of the central recirculation bubble and the extension of the recirculation at the edge of the pipe expansion is in good agreement with the measured results.

The measured cross-sectional profiles of the three velocity components are compared with the calculations in figure 15 for case 2. The agreement is very good, except for the tangential velocity

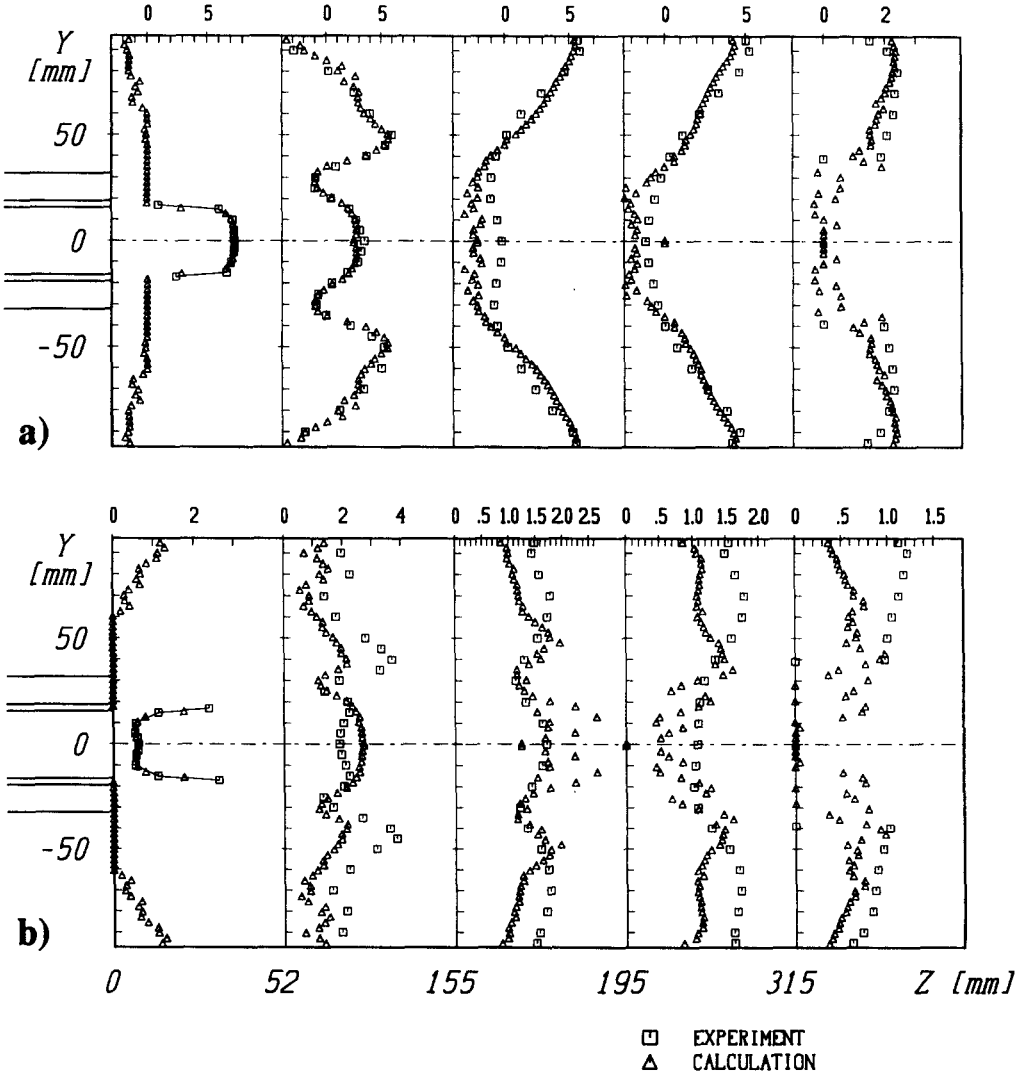

Figure 16. Measured and calculated axial particle velocity (m/s): (a) mean velocity; (b) velocity fluctuation.

which is underpredicted in the region downstream of the location where the recirculation bubble has its largest radial extension. Although, the turbulent kinetic energy of the gas phase is considerably underpredicted in the initial mixing region between the primary and annular jets and within the recirculation at the edge of the pipe expansion ($z = 52$ mm), the agreement is reasonably good for the cross-sections further downstream. Similar results have been obtained for swirl case 1 which were summarized in a previous publication (Sommerfeld *et al.* 1992).

The measured and calculated particle mean velocities and the associated velocity fluctuations are compared in figures 16 and 17. All mean velocity components are generally well-predicted, except for the radial velocity which is predicted to be positive at $z = 315$ mm (i.e. the particles move towards the wall) whereas the experiments show negative velocities. This implies that in the experiment the particles move on average away from the wall. Although, it might be expected that the numerical results in the near-wall region are very sensitive with respect to the modelling of the wall collision process, it was found that a variation in the normal restitution ratio and the friction coefficient in the three-dimensional inelastic collision model did not result in considerable changes in the velocity profiles. The scattering of the numerical results in the core region downstream of the location, where the central recirculation bubble has its largest radial extension, is a result of the low number of sampled particles, since the majority of the particles have already moved out of the core region [see figure 6(b)].

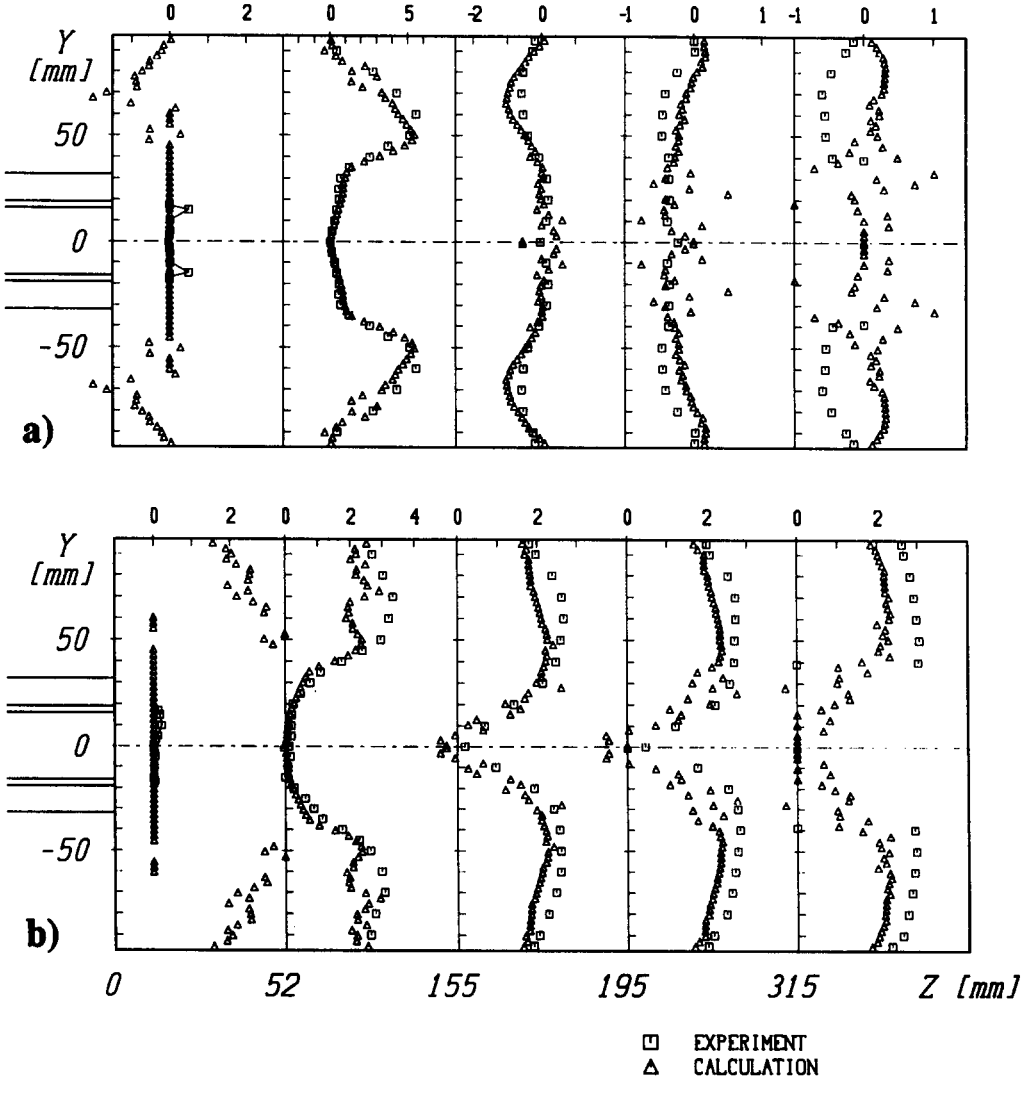

Figure 17. Comparison of measurements and calculations: (a) radial particle velocity (m/s); (b) tangential particle velocity (m/s).

The particle velocity fluctuations are more or less underpredicted for all three velocity components, which presumably is caused by the underprediction of the gas-phase turbulent kinetic energy in the initial region of flow development [see figure 15(d)]. This is demonstrated in figure 16(b) for the fluctuation of the axial particle velocity component.

The calculated particle mass flux shows very good agreement with the experiments in the initial region just downstream of the inlet, namely at $z = 52$ mm, and further downstream at $z = 315$ [figure 18(a)]. In the intermediate region, where the particles rebound from the wall and interact again with the central recirculation bubble (see figure 6), some differences between the experiments and predictions are observed in the near-wall region. At $z = 155$ and 195 mm, the measurements show a relatively narrow layer of particles near the wall with the maximum being directly at the wall. The calculations show a slightly wider particle layer with a maximum in the particle mass flux located at a radial position of 65 mm, which might result from the assumptions made in the particle–wall collision model.

A sensitivity study, by using different normal restitution ratios and wall friction coefficients in the particle–wall collision model, shows that their influence on the particle mass flux distribution at $z = 155$ and 195 mm is not too strong (figure 19). A reduction in the normal restitution ratio from 0.8 to 0.6 gives a slightly narrower particle layer with a more pronounced maximum closer

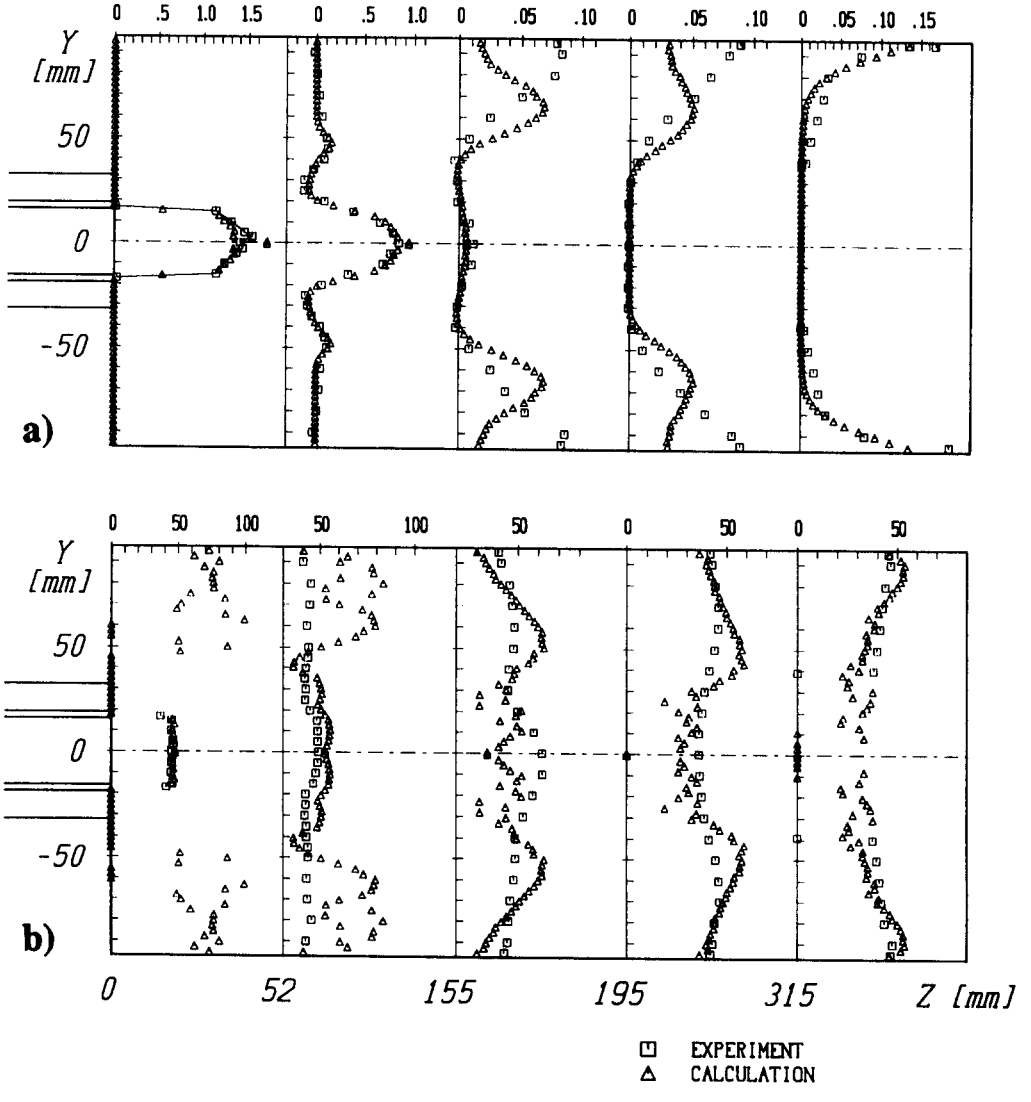

Figure 18. Comparison of measurements and calculations: (a) axial particle mass flux (kg/m^2 s); (b) particle mean number diameter (μm).

to the wall. When the particle lift force is switched off in the calculations, the particle layer becomes wider with a less pronounced maximum in the mass flux distribution near the wall. This also shows that the particle lift force due to rotation is only important in the near-wall region, where high rotational velocities are induced by the wall collision. Since the particles lag behind the air flow in the near-wall region, the direction of the lift force is directed towards the centreline. From these results, one may conclude that the particle motion in the near-wall region might also be affected by electrostatic forces, although the Plexiglas test section was carefully grounded.

The predicted distribution of the particle mean number diameter throughout the flow field shows some larger differences when compared to the measurements [figure 18(b)]. In particular, in the recirculation of the pipe expansion (see $z = 52$ mm) the calculated mean particle diameter is much larger than observed in the experiment. It should, however, be noted that the mean particle size is the most sensitive parameter to be predicted. It requires correct predictions of the evolution of the particle size distributions and the correlation between size and velocity, which is a result of the particles response to the mean flow and turbulence.

The comparison of the measured and calculated particle size–velocity correlations for several locations in the flow shows, in general, reasonable agreement (figure 20). The measured development of the size–velocity correlation along the centreline within the recirculation bubble shows the increasing number of particles with negative axial velocities and the shift of the size distribution towards larger particles. At the location $z/x = 155/20$ another group of small particles (i.e. between 15–30 μm) with high negative velocities appears in the size–velocity correlation. These particles are coming from further downstream after they have rebounded from the wall and been entrained in the recirculation region. The predictions show the same trends in the core region of the recirculation bubble but the size distribution is shifted towards larger particles as compared to the experiments, which also results in a larger particle mean number diameter [see figure 18(b)]. At other locations in the flow field the agreement between the experiments and numerical calculations is considerably better.

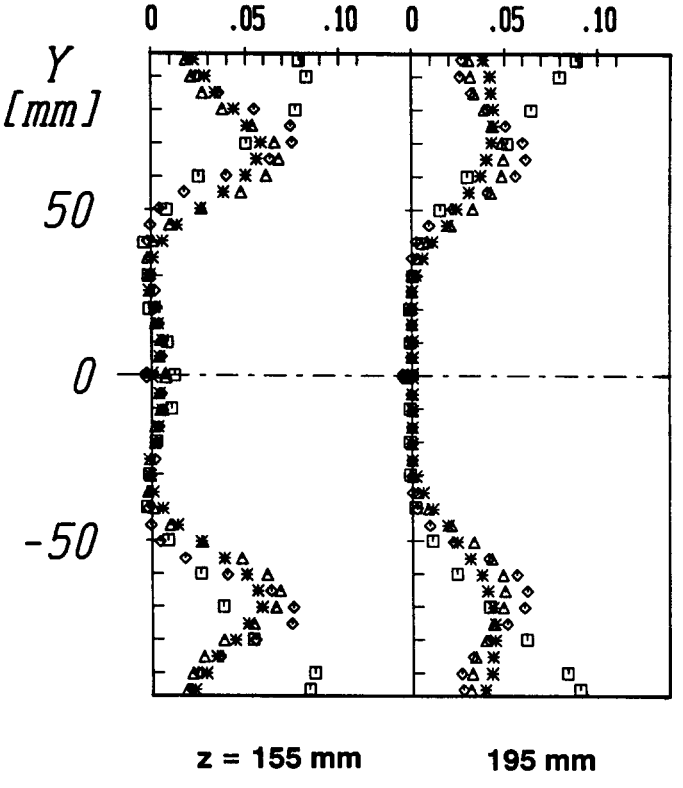

Figure 19. Measured and calculated axial particle mass flux at $z = 115$ and 195 mm for different parameters in the wall collision model: △, with lift force, $e = 0.8$, $\mu = 0.3$; ◇, with lift force, $e = 0.6$, $\mu = 0.3$; *, without lift force, $e = 0.8$, $\mu = 0.3$; □, experiment.

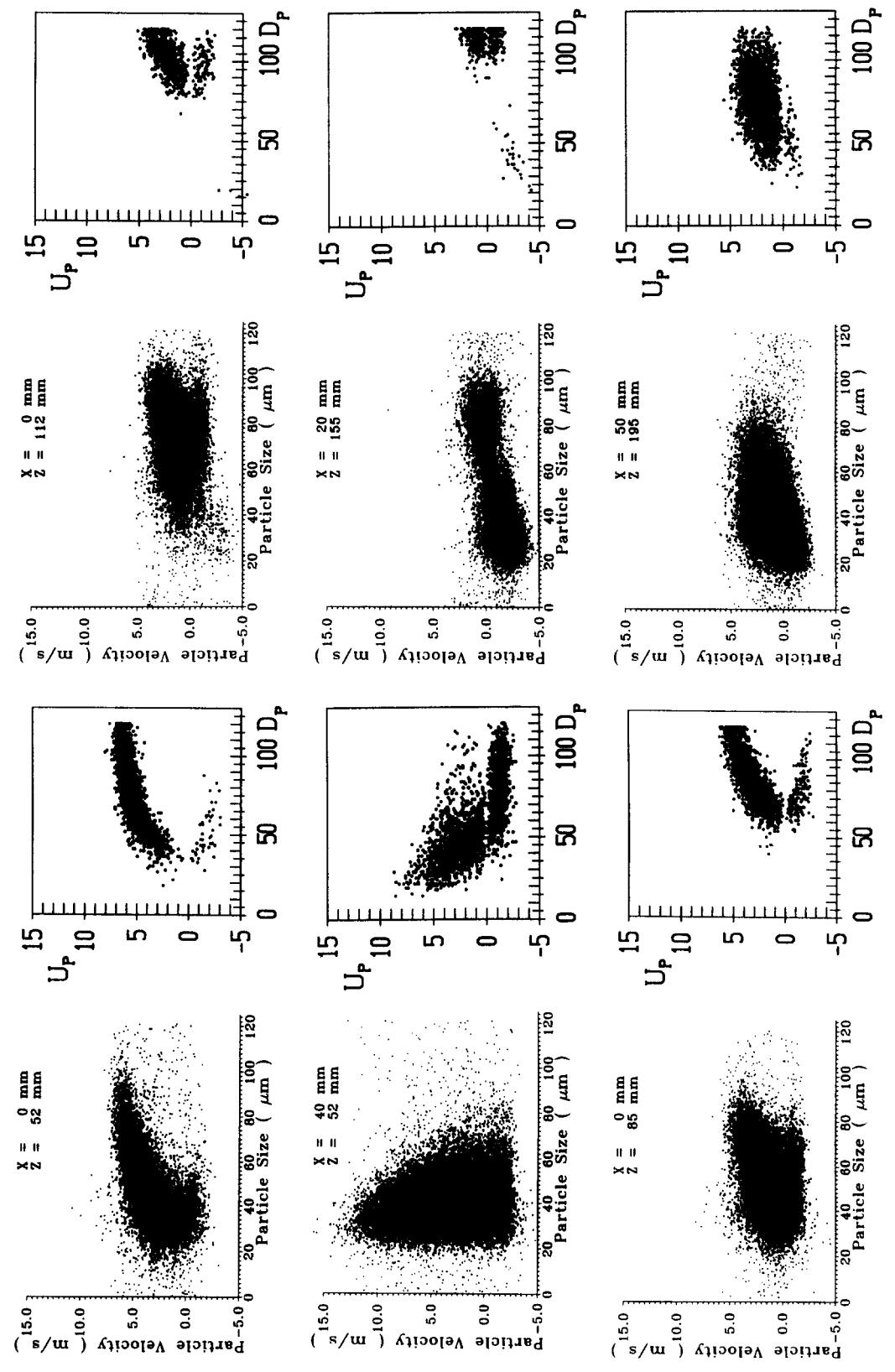

Figure 20. Comparison between measured and calculated particle size–velocity correlations at various locations in the flow field.

CONCLUSIONS

The particle behaviour in a confined swirling flow was studied experimentally by applying PDA and numerically by the Eulerian/Lagrangian method for the gas and particle phases, respectively.

Although the PDA technique already yields detailed information on the evolution of the particle size distribution and the correlation between size and velocity throughout the flow field, additional insight into the particle motion in this complex can be gained by numerical calculations. Furthermore, it was possible to determine the particle residence times numerically for the two flow conditions considered. The main conclusions from the studies are:

- The inertia of the particles interacting with the established central recirculation bubble results in a separation of the particle phase. This implies that large particles penetrate a large portion of the central recirculation bubble, while small particles respond to the flow reversal in the upper region of the recirculation bubble and are then entrained into the air stream coming from the annular inlet.
- A decrease in the particle injection velocity at the primary jet gives more time for the large particles to respond to the flow reversal. Therefore, a larger amount of recirculating particle mass within the central reverse flow region is established compared to in cases with high injection velocities.
- The numerical calculations for both the gas flow and the particle phase show good agreement with the experiments, although minor differences were found for the particle mass flux and the profiles of the particle mean number diameter. It should, however, be noted that the general trends are predicted reasonably well and that these are some of the first numerical predictions where the spatial change in the particle size distribution was considered in a complex gas–solid flow.
- The underpredictions of both the gas turbulence and the particle velocity fluctuations are inherent to the k–ϵ turbulence model, although the agreement with the measurements is surprisingly good. It is, however, supposed that the application of Reynolds stress models could improve these shortcomings.
- The predictions of the correlation between particle size and velocity showed reasonable agreement with the measurements for the majority of locations within the flow field. This demonstrates that the modified "eddy lifetime" particle dispersion model, which takes into account the non-homogeneity of the flow turbulences, performs quite well.
- Furthermore, it was possible in the numerical calculations to determine the correlation between particle size and residence time within the central recirculation bubble. The results demonstrate that the particle residence time can be adjusted according to the requirements of the application by changing the particle injection velocity through the primary jet. For low particle injection velocities, the residence time of the larger particles could be considerably increased. This information is especially useful for the design of burners in order to guarantee the burnout of the larger fuel particles or droplets.
- The numerical calculations, furthermore, revealed that the motion of the particles, after their first interaction with the central recirculation bubble, is strongly influenced by particle–wall collisions and the resulting high particle rotation gives rise to transverse lift forces. Therefore, a three-dimensional inelastic particle–wall collision model was included in the calculations. But further improvements to the wall–collision model are required based on a detailed analysis of the collision of spherical particles with Plexiglas walls.
- Based on the dimensions of the central recirculation bubble, the particle injection velocity and the magnitude of reverse flow, the particle response characteristics in a swirling flow with a central recirculation bubble were defined by introducing two time-scale ratios which determine the particle behaviour in the different flow regions.

Acknowledgements—The experimental and numerical studies were performed within the framework of the project "Heterogeneous combustion in swirling flows: particle dispersion with heat and mass transfer". The financial support for this project from the Stiftung Volkswagenwerk is gratefully acknowledged. Furthermore, the authors would like to thank A. Ando who modified the Lagrangian particle tracking code for swirling flows.

REFERENCES

ALTGELD, H., JONES, W. P. & WILHELMI, J. 1983 Velocity measurements in a confined swirl driven recirculating flow. *Expts Fluids* **1,** 73–78.

BLÜMCKE, E., EICKHOFF, H. & HASSA, C. 1988 Dispersion of monosized droplets in a turbulent swirling flow. In *Proc. 4th Int. Conf. on Liquid Atomization and Spray Systems*, pp. 89–96.

BRENA DE LA ROSA, A., WANG, G. & BACHALO, W. D. 1992 The effect of swirl on the velocity and turbulence fields of a liquid spray. *Trans. ASME Jl Engng Gas Turb. Power* **114,** 72–81.

BRUM, R. D. & SAMUELSEN, G. S. 1987 Two-component laser anemometry measurements of non-reacting and reacting complex flows in a swirl-stabilized model combustor. *Expts Fluids* **5,** 95–102.

BULZAN, D. L., SHUEN, J.-S. & FAETH, G. M. 1988 Particle laden weakly swirling free jets: measurements and predictions. AIAA Paper 88-3138.

DELLENBACK, P. A., METZGER, D. E. & NEITZEL, G. P. 1988 Measurements in turbulent swirling flow through an aprupt axisymmetric expansion. *AIAA Jl* **26,** 669–681.

DOMNICK, J., ERTEL, H. & TROPEA, C. 1988 Processing of phase/Doppler signals using the cross spectral density function. In *Proc. 4th Int. Symp. on Applications of Laser Anemometry to Fluid Mechanics*, Paper 3.8.

DURST, F. & WENNERBERG, D. 1991 Numerical aspects on calculation of confined swirling flows with internal recirculation. *Int. J. Numer. Meth. Fluids* **12,** 203–224.

ESCUDIER, M. P. & KELLER, J. J. 1985 Recirculation in swirling flow: a manifestation of vortex breakdown. *AIAA Jl* **23,** 111–116.

FU, S., HUANG, P. G., LAUNDER, B. E. & LESCHZINER, M. A. 1988 A comparison of algebraic and differential second-moment closures for axisymmetric turbulent shear flows with and without swirl. *Trans. ASME Jl Fluids Engng* **110,** 216–221.

GOSMAN, A. D. & IOANNIDES, E. 1983 Aspects of computer simulation of liquid-fueled combustors. *J. Energy* **7,** 482–490.

HALLETT, W. L. H. & TOEWS, P. J. 1987 The effect of inlet conditions and expansions ratio on the onset of flow reversal in swirling flow in a sudden expansion. *Expts Fluids* **5,** 129–133.

HARDALAPAS, Y., TAYLOR, A. M. K. P. & WHITELAW, J. H. 1990 Velocity and size characteristics of liquid-fuelled flames stabilized by a swirl burner. *Proc. R. Soc. Lond.* **A428,** 129–155.

HOGG, S. I. & LESCHZINER, M. A. 1989 Computations of highly swirling confined flow with a Reynolds stress turbulence model. *AIAA Jl* **27,** 57–63.

LILLEY, D. G. 1977 Swirl flow in combustion: a review. *AIAA Jl* **15,** 1063–1078.

MILOJEVIC, D. 1990 Lagrangian stochastic–deterministic (LSD) prediction of particle dispersion in turbulence. *Particles Particle Syst. Charact.* **7,** 181–190.

PRÖBSTLE, G. & WENZ, W. 1988 Velocity measurements in a swirl driven pulverized coal combustion chamber. *Combust. Flame* **72,** 193–203.

QIU, H.-H., SOMMERFELD, M. & DURST, F. 1991 High resolution data processing for phase-Doppler measurements in a complex two-phase flow. *Measur. Sci. Technol.* **2,** 455–463.

RHODE, D. L., LILLEY, D. G. & MCLAUGHLIN, D. K. 1983 Mean flow field in axisymmetric combustor geometries with swirl. *AIAA Jl* **21,** 593–600.

RUBINOW, S. I. & KELLER, J. B. 1961 The transverse force on spinning sphere moving in a viscous fluid. *J. Fluid Mech.* **11,** 447–459.

SMART, J. P. & WEBER, R. 1989 Reduction of NO_x and optimisation of burnout with an aerodynamically air-staged burner and an air-staged compressor burner. *J. Inst. Energy* **62,** 237–245.

SOMMERFELD, M. 1990 Particle dispersion in turbulent flow: the effect of particle size distribution. *Particles Particle Syst. Charact.* **7,** 209–220.

SOMMERFELD, M. & KREBS, W. 1990 Particle dispersion in a swirling confined jet flow. *Particles Particle Syst. Charact.* **7,** 16–24.

SOMMERFELD, M. & QIU, H.-H. 1991 Detailed measurements in a swirling particulate two-phase flow by a phase-Doppler anemometer. *Int. J. Heat Fluid Flow* **12,** 20–28.

SOMMERFELD, M., QIU, H.-H. & KOUBARIDIS, D. 1991 The influence of swirl on the particle dispersion in a pipe expansion flow. In *Applications of Laser Techniques to Fluid Mechanics, 5th International Symposium, Lisbon 1990* (Edited by ADRIAN, R. J., DURAO, D. F. G., DURST, F., MAEDA, M. & WHITELAW, J. H.), pp. 142–162. Springer-Verlag, Berlin.

SOMMERFELD, M., ANDO, A. & WENNERBERG, D. 1992 Swirling, particle-fiaden flows through a pipe expansion. *Trans. ASME Jl Fluids Engng* **114,** 648–656.

SYRED, N. & BEER, J. M. 1974 Combustion in swirling flow: a review. *Combust. Flame* **23,** 143–201.

THIELEN, W. 1988 Einfluss der Brennerkonstruktion auf das brennernahe Stömungsfeld in gestuften Kohlestaubfeuerungen. *Brennst. Wärme Kraft* **40,** 186–192.

TSUJI, Y., OSHIMA, T. & MORIKAWA, Y. 1985 Numerical simulation of pneumatic conveying in a horizontal pipe. *KONA* **3,** 38–51.

WEBER, R., VISSER, B. M. & BOYSAN, F. 1990 Assessment of turbulence modeling for engineering predictions of swirling vortices in the near burner zone. *Int. J. Heat. Fluid Flow* **11,** 225–235.